Targeting the Mitochondrial ACSS1-Dependent Acetate–Pyrimidine Axis Suppresses Mantle Cell Lymphoma Progression

Johnvesly Basappa[1*], Aaron R. Goldman[2], Cosimo Lobello[1], Shengchun.Wang[1], David Rushmore[1], Olga Melnikov[1], Neil V. Sen[1], Vinay S. Mallikarjuna[1], Priyanka Jain[1], Masoud Edalati[1], David S Nelson[4], Kathy Q. Cai[1], Pin Lu[1], Reza Nejati[1], Hossein Borghaei[1], Pradeep K Gupta[4], Kavindra Nath[4], Kathryn E. Wellen[3] and Mariusz A. Wasik[1]

[1]Fox Chase Cancer Center, Philadelphia, PA, USA

[2]Proteomics & Metabolomics Facility, Wistar Institute, Philadelphia, PA, USA Philadelphia, PA

[3]Department of Cancer Biology, University of Pennsylvania Perelman School of Medicine, Philadelphia, PA, USA.

[4]Department of Radiology, University of Pennsylvania, Philadelphia, PA.

Short title: ACSS1 Overexpression Drives Acetate-Dependent Metabolic Reprogramming in MCL

Keywords: *ACSS1*, ACSS2, ACLY, CAD, DHODH, acetate metabolism, oncometabolite, cancer metabolism,

*** Corresponding author:**

Johnvesly Basappa, Ph.D.

Department of Pathology, Fox Chase Cancer Center, Philadelphia, PA

Email: Johnvesly.Basappa@fccc.edu

Phone: 215-728-3039

Declaration of interest statement:

The authors declare that there are no relevant financial or non-financial competing interests to report.

Abstract

Acetate serves as an alternative carbon source in nutrient-limited tumors, yet its role in supporting nucleotide biosynthesis remains poorly understood. Here, we identify the mitochondrial enzyme ACSS1 as a key metabolic driver in mantle cell lymphoma (MCL), diffuse large B-cell lymphoma (DLBCL), and chronic lymphocytic leukemia (CLL). ACSS1 is frequently overexpressed and catalyzes the conversion of acetate to mitochondrial acetyl-CoA, sustaining oxidative metabolism and biosynthesis under nutrient stress. Genetic silencing of ACSS1 impairs mitochondrial respiration and disrupts acetate incorporation into acetyl-CoA, TCA cycle intermediates, glutamate, and aspartate, while markedly reducing ^{13}C-acetate labeling of dihydroorotate and orotate, intermediates in de novo pyrimidine synthesis. Untargeted metabolomics reveal enrichment of pyrimidine biosynthesis pathways in ACSS1-high cells. Notably, acetate or uridine supplementation rescues the growth of ACSS1-deficient cells, confirming a functional link between acetate metabolism and nucleotide synthesis. Importantly, *in vivo* studies using luciferase-labeled JeKo-1 and Maver mantle cell lymphoma xenografts demonstrate that ACSS1 knockdown significantly suppresses tumor growth. NSG mice injected with ACSS1-silenced cells exhibit a marked reduction in tumor burden, as measured by bioluminescence imaging and total photon flux, with significant differences observed at days 14 and 21 post-injection. These findings establish that ACSS1 is required not only for metabolic adaptation *in vitro* but also for lymphoma progression *in vivo*. Collectively, our results uncover an ACSS1-dependent mitochondrial acetate–pyrimidine axis that sustains lymphoma growth and represents a previously unrecognized therapeutic vulnerability.

Statement of Significance

This study identifies ACSS1 as a critical metabolic vulnerability in mantle cell lymphoma (MCL), linking mitochondrial acetate metabolism to de novo pyrimidine biosynthesis and tumor progression. We demonstrate that ACSS1 is frequently overexpressed in MCL and is essential for converting acetate into mitochondrial acetyl-CoA, thereby sustaining TCA cycle activity, nucleotide production, and cell survival under nutrient stress. Loss of ACSS1 disrupts this acetate–pyrimidine axis, impairing oxidative metabolism and reducing lymphoma cell viability in vitro. Importantly, ACSS1 silencing significantly suppresses tumor growth in vivo, establishing its requirement for lymphoma progression. The ability of acetate or uridine supplementation to rescue ACSS1-deficient cells further highlights the functional coupling between mitochondrial acetate utilization and nucleotide synthesis. Together, these findings reveal a previously unrecognized mechanism of metabolic adaptation in aggressive lymphomas and offer ACSS1-mediated acetate metabolism as a promising therapeutic target.

Introduction

In higher vertebrates, the swift growth of cells mainly relies on the intake of glucose and glutamine(1). Acetate is another nutritional source vital for the progression of many cancers, which often exhibit dysregulated metabolism, and it is essential under nutrient-deprived conditions(2). The mitochondrial acetyl-CoA synthetase short-chain family member 1 (ACSS1) catalyzes acetate, an energy source during nutrient deprivation conditions, to produce mitochondrial acetyl-CoA(2, 3). A recent study suggests that acetate promotes PD-L1 expression and immune evasion by upregulating c-Myc(4). Indeed, in ketogenic conditions, such as prolonged fasting or diabetes, the liver also generates sufficient quantities of acetate and releases it into the bloodstream(5). Mammals have three isoforms of the short-chain acetyl-CoA synthetases family: ACSS1, ACSS2, and ACSS3, which convert acetate into acetyl-CoA(6, 7), which is essential for cell growth and proliferation(8, 9). ACSS1 and ACSS3 localize in the mitochondria, while ACSS2 is found in the nucleus and cytoplasm(10). Among the three isoforms, ACSS2's role in acetate metabolism and cancer progression has been extensively studied in various types of cancer, including pancreatic cancer(11), hepatocellular carcinoma(12, 13), glioblastoma(14), breast cancer(15), prostate cancer(15), bladder cancer(16) and cervical squamous cell carcinoma(17). ACSS1 plays a crucial role in thermogenesis during fasting, in low-glucose or ketogenic states, and is vital for survival(18). The expression of ACSS1 is regulated in an estrogen receptor-dependent manner, and the estrogen hormone plays a role in regulating the incorporation of acetate into DNA(19, 20). In highly oxygen-rich environments, most acetyl-CoA is generated via the glucose pathway. Conversely, during low oxygen conditions, acetate serves as a source for acetyl-CoA production(21). The exact function of mitochondrial ACSS1 in acetate metabolism within lymphoma remains unknown.

Mantle cell lymphoma (MCL) is a type of B-cell lymphoma, characterized by a median overall survival of just 3-5 years (22). While a subset of patients with mantle cell lymphoma (MCL) initially respond to Bruton tyrosine kinase (BTK) inhibitors, resistance, either intrinsic or acquired, is a common clinical challenge. Emerging evidence suggests that metabolic reprogramming toward oxidative phosphorylation (OXPHOS) contributes to disease progression and therapeutic resistance in MCL. In this study, we employed MCL cell

97 lines as a model to investigate the role of ACSS1 in acetate metabolism under nutrient-deprived conditions.
98 Using extensive ^{13}C-acetate stable isotope tracing and genetic knockdown of ACSS1, we uncover a
99 previously unrecognized function of ACSS1 in supporting acetate-fueled survival and de novo pyrimidine
100 synthesis. These findings highlight ACSS1 as a critical mediator of metabolic adaptation in aggressive,
101 therapy-resistant MCL.
102
103 **Results**
104 **ACSS1 expression shows variable expression in MCL and DLBCL samples**
105 To validate ACSS1 protein expression in clinical samples, we performed immunohistochemistry (IHC) on
106 tumor tissue microarrays (TMAs) from mantle cell lymphoma (MCL) patient biopsies (n = 27) obtained
107 from Fox Chase Cancer Center. ACSS1 staining was detected in 92.6% of MCL cases (25/27), with
108 expression levels categorized as strong in 7 cases (25.9%), moderate in 9 cases (33.3%), and weak in 9
109 cases (33.3%) (Fig. 1A, B). A representative low-magnification image of the TMA block is shown in
110 Supplementary Fig. 1A. In chronic lymphocytic leukemia (CLL) patient samples (n = 13), IHC analysis
111 revealed ACSS1 expression in 7 cases (53.8%), as shown in Supplementary Fig. 1A. We next evaluated
112 diffuse large B-cell lymphoma (DLBCL) samples (n = 44). We observed ACSS1 positivity in 35 cases
113 (79.5%) (Fig. 1C), including strong expression in 6 cases (13.6%), moderate in 14 (31.8%), and weak in 15
114 (34.1%) (Fig. 1D). The corresponding TMA overview is provided in Supplementary Fig. 1B. These data
115 confirm frequent ACSS1 protein expression across multiple B-cell malignancies, consistent with
116 transcriptomic analyses.
117 To validate the specificity of the ACSS1 antibody for IHC staining, a breast cancer sample was tested using
118 immunofluorescence with ACSS1 and the mitochondrial marker VDAC1(Supplementary Fig. 2A). The
119 negative control shows no signal for ACSS1 staining (Supplementary Fig. 2B). To confirm ACSS1
120 expression in mitochondria, we performed fractionation on MCL cell lines Maver and Jeko-1.
121 Immunoblotting revealed that ACSS1 is primarily located in mitochondria (Supplementary Fig. 2C).
122

123 To further investigate the ACSS1 expression in various cancer models, we analyzed publicly available
124 RNA-seq data from hematological malignancy cell lines using the Expression Atlas
125 (https://www.ebi.ac.uk/gxa/home). This analysis focused on hematopoietic and lymphoid-derived cancer
126 models, including mantle cell lymphoma (MCL), diffuse large B-cell lymphoma (DLBCL), chronic
127 lymphocytic leukemia (CLL), acute myeloid leukemia (AML), and anaplastic large cell lymphoma
128 (ALCL). Among acetyl-CoA synthetases, mitochondrial ACSS1 exhibited notably high expression in non-
129 Hodgkin lymphoma (NHL) cell lines and patient-derived samples. In contrast, ACSS3 expression was
130 negligible across all profiled lines (Supplementary Fig. 3A, B). To extend these observations, we examined
131 the expressions of ACSS1 and ACSS2 in hematopoietic and lymphoid malignancies using The Cancer
132 Genome Atlas (TCGA). ACSS1 was overexpressed in 36.2% of 221 hematopoietic and lymphoid samples,
133 with only 1.36% showing reduced expression (Table 1). Given the limited characterization of ACSS1 in
134 solid tumors, we further assessed its expression across multiple cancer types using TCGA. ACSS1 was
135 significantly overexpressed relative to matched normal tissue in several malignancies, including lung
136 (10.89%), ovarian (29.32%), prostate (16.47%), central nervous system (79.91%), cervical (84.04%), large
137 intestine (25.9%), and head and neck squamous cell carcinoma (24.71%) (Table 1). These findings suggest
138 that ACSS1 upregulation is a recurrent feature across both hematological and solid tumors, highlighting its
139 potential role in cancer-associated acetate metabolism.
140

141 **Acetate feeds the TCA cycle in MCL and DLBCL cells in an ACSS1-dependent manner**

142 Our analysis of patient-derived TMA, TCGA data, and hematological cancer cell lines revealed variable
143 ACSS1 expression across mantle cell lymphoma (MCL) and diffuse large B-cell lymphoma (DLBCL)
144 models. Notably, ACSS1 mRNA levels were low in MCL-RL cells but were significantly elevated in Jeko-
145 1 and Maver MCL cell lines, exhibiting 18-fold and 24-fold higher expression, respectively (Fig. 2A). In
146 contrast, ACSS2 expression remained low and was not differentially expressed across these MCL lines
147 (Fig. 2B). Similarly, high ACSS1 mRNA levels were observed in DLBCL cell lines, whereas one cell line
148 OCI-LY1 displayed low ACSS1 expression (Fig. 2C). Consistent with MCL, ACSS2 expression was

149 uniformly low in DLBCL lines (Fig. 2D). Immunoblot analysis of five MCL cell lines (Jeko-1, Maver,
150 Mino, Granta-519, and RL) confirmed robust ACSS1 protein expression in all except MCL-RL cells (Fig.
151 2E). Likewise, immunoblotting of four DLBCL cell lines demonstrated elevated ACSS1 protein levels in
152 all except OCI-LY1 cells (Fig. 2F). These findings suggest that ACSS1 expression correlates with variable
153 expressions in both MCL and DLBCL models.
154 To investigate the relationship between ACSS1 expression and acetate metabolism, we performed stable
155 isotope tracing using ^{13}C-labeled acetate, followed by liquid chromatography–mass spectrometry (LC-MS)
156 to analyze mass isotopologue distributions (MIDs) of tricarboxylic acid (TCA) cycle intermediates as
157 illustrated in schematics (Fig. 2G). Stable isotope tracing with ^{13}C-labeled acetate revealed distinct
158 differences in acetate utilization correlated with ACSS1 expression levels. Analysis of acetyl-CoA mass
159 isotopologue distributions showed significant variation in both unlabeled and labeled species among the
160 three MCL cell lines (Fig. 2H). To further assess the metabolic fate of acetate-derived carbon, we quantified
161 the incorporation of ^{13}C into tricarboxylic acid (TCA) cycle intermediates, including citrate, α-ketoglutarate
162 (α-KG), succinate, and malate. Citrate labeling patterns differed markedly among RL, Jeko-1, and Maver
163 cells, with Jeko-1 and Maver cells exhibiting significantly increased ^{13}C-acetate–derived labeling compared
164 with RL cells ($p < 0.0001$) (Fig. 2I). Similarly, α-KG showed significant differences in M+2, M+3, M+4,
165 and M+5 isotopologues, particularly between Jeko-1/Maver and the low-ACSS1 RL cells (Fig. 2J). These
166 trends were also observed in succinate (Fig. 2K) and malate (Fig. 2L), with higher ^{13}C incorporation in
167 Jeko-1 and Maver relative to RL. Collectively, these findings indicate that elevated ACSS1 expression
168 enhances acetate utilization and contributes to increased TCA cycle flux in MCL cell lines.
169 To elucidate the role of ACSS1 in mitochondrial acetate metabolism, we silenced ACSS1 in two MCL cell
170 lines, Jeko-1 and Maver, which exhibit high endogenous ACSS1 expression. Knockdown efficiency was
171 confirmed at the transcript and protein levels using quantitative PCR and immunoblotting, respectively
172 (Fig. 2M, N). To determine whether ACSS1 drives mitochondrial acetate metabolism, we conducted ^{13}C-
173 acetate labeling analysis in both shControl and ACSS1 knockdown (shACSS1) cell lines, as illustrated in
174 the schematic (Fig. 2O). Given that most mammalian cells rely primarily on glucose and glutamine for

175 energy production, we hypothesized that ACSS1 is particularly critical under nutrient-deprived conditions.
176 Cells were cultured for 24 hours in ^{13}C-acetate–supplemented RPMI medium lacking glucose and
177 glutamine, with 1% dialyzed FBS. Metabolomic analysis revealed a significant reduction in acetyl-CoA
178 labeling in ACSS1 knockdown Jeko-1 cells $p < 0.0001$(Fig. 2P). To distinguish between cytosolic and
179 mitochondrial acetyl-CoA pools, we quantified mitochondrial acetylcarnitine labeling. ACSS1 knockdown
180 led to a marked reduction in acetylcarnitine M+2 labeling in both Jeko-1 (>40%; $p < 0.0003$) and Maver (
181 $p < 0.0005$) cells (Fig. 2Q), supporting a key role for ACSS1 in mitochondrial acetate utilization. Further
182 analysis of ^{13}C-acetate–derived MIDs in TCA cycle intermediates demonstrated that ACSS1 knockdown
183 decreased citrate M+2–M+5 labeling in both cell lines, consistent with reduced carbon entry from acetate
184 through multiple TCA cycle turns (Fig. 2R). Additional intermediates including aconitate, α-ketoglutarate,
185 and malate exhibited similar reductions in ^{13}C labeling upon ACSS1 silencing (Fig. 2S-U). These results
186 collectively indicate that ACSS1 is essential for converting acetate into mitochondrial acetyl-CoA, fueling
187 oxidative phosphorylation via the TCA cycle, particularly under nutrient-limited conditions. Thus, ACSS1
188 supports mitochondrial bioenergetics in MCL cells with elevated ACSS1 expression.
189 Building on the observed role of ACSS1 in mitochondrial acetate metabolism and its influence on TCA
190 cycle activity, we hypothesized that ACSS1 also modulates oxidative phosphorylation (OXPHOS) through
191 regulation of oxygen consumption rate (OCR). To evaluate this, we measured basal OCR in glucose-starved
192 RL (low ACSS1-expressing), Jeko-1, and Maver (high ACSS1-expressing) MCL cell lines following
193 exposure to 1 mM acetate. Acetate supplementation led to a significant increase in OCR in Jeko-1 (24%, P
194 < 0.002) and Maver (30%, $P < 0.0001$) cells. In contrast, RL cells exhibited minimal response (Fig. 2V).
195 These findings suggest that ACSS1 expression enables acetate-fueled mitochondrial respiration under
196 glucose-limiting conditions. To further confirm the role of ACSS1 in regulating acetate-dependent
197 OXPHOS, we compared OCR in control (shCon) and ACSS1 knockdown (shACSS1) Jeko-1 and Maver
198 cells. In both cell lines, ACSS1 silencing resulted in a marked reduction in basal and stress-induced OCR
199 compared to control cells (Fig. 2W, X), indicating that ACSS1 is critical for sustaining mitochondrial

respiration in the presence of acetate. Collectively, these results underscore the importance of ACSS1 in driving acetate-supported oxidative metabolism in MCL cells.

ACSS1 supports pyrimidine metabolism

Based on the differential expression of ACSS1 in MCL cell lines high in Jeko-1 and Maver, and low in RL we aimed to investigate ACSS1's role in acetate metabolism under nutrient-deprived conditions. To do this, we performed ^{13}C-acetate tracing in these cell lines. Our metabolic analysis, which examined changes in steady-state metabolite pathways and enrichment patterns, revealed perturbations in pyrimidine biosynthesis pathways. To determine whether acetate directly contributes to pyrimidine biosynthesis, we analyzed the incorporation of ^{13}C into key metabolic precursors, as illustrated in the schematic (Fig. 3A). In Jeko-1 and Maver cells, which express high levels of ACSS1, we observed a significant increase in ^{13}C-acetate–derived M+2 to M+5 labeling of aspartate and glutamate two critical intermediates for de novo pyrimidine synthesis compared to low-ACSS1-expressing RL cells ($P < 0.0001$, Fig. 3B, C). These findings indicate that ACSS1 enhances pyrimidine biosynthesis by supporting the generation of TCA cycle–derived intermediates under acetate-reliant, nutrient-limited conditions. To further evaluate acetate's contribution to pyrimidine synthesis, we examined the labeling patterns in downstream intermediates. Isotope tracing revealed a significant enrichment of M+2 to M+5 ^{13}C-labeled orotate, UMP, UDP, and CDP in Jeko-1 and Maver cells compared to RL ($P < 0.0001$, Fig. 3D–G), further supporting a model in which ACSS1 drives acetate-dependent pyrimidine biosynthesis.

Next, we hypothesized that overexpression of ACSS1 in Jeko-1 and Maver cell lines drives acetate metabolism in MCL. To investigate this, we silenced ACSS1 expression in both cell lines using lentiviral short hairpin RNA (shRNA) targeting ACSS1. The resulting shACSS1 and shCon cell lines were subsequently used in ^{13}C-acetate tracing experiments to assess alterations in acetate metabolism. Our metabolomics analysis data showed a highly significant reduction in M+2 to M+5 ^{13}C-labeling of aspartate and glutamate in shACSS1 Jeko-1 and Maver cells compared to shCon ($P < 0.0001$, Fig. 3H, I). Next, ^{13}C-acetate isotope tracing revealed a significant reduction in M+2 to M+5 ^{13}C-labeled dihydroorotate and

226 orotate in shACSS1 Jeko-1 and Maver cells compared to scramble controls ($P < 0.0001$, Fig. 3J, K).
227 Comparative analysis of shACSS1 and shCon Jeko-1 and Maver cells cultured with ^{13}C-acetate revealed
228 significant alterations in cellular metabolism. Of the 206 metabolites analyzed, 46 metabolites were
229 significantly changed (absolute fold change >1.5, $P < 0.05$), with the majority associated with the
230 pyrimidine synthesis pathway (Supplementary Fig. 4A, B). A subset of altered pyrimidine metabolites from
231 Jeko-1 cells is highlighted in Fig. 3L. Additionally, pathway and enrichment analyses confirmed the
232 enrichment of metabolites linked to pyrimidine biosynthesis (Fig. 3M, N). These findings suggest that
233 ACSS1 plays a critical role in channeling acetate-derived carbon into TCA cycle intermediates that support
234 de novo pyrimidine synthesis.
235 We hypothesized that silencing ACSS1 in Jeko-1 cells would impact the expression of key enzymes
236 involved in pyrimidine biosynthesis, as illustrated in the schematic (Fig. 3O). To test this, we isolated RNA
237 from shCon and shACSS1 cells cultured in complete media and performed quantitative RT-PCR to assess
238 the expression of CAD and DHODH. The results demonstrated altered expression of both genes in
239 shACSS1 cells compared to shCon (Fig. 3P). To further evaluate these findings at the protein level, we
240 conducted Western blot analysis under different nutrient conditions. Notably, shACSS1 cells exhibited
241 reduced CAD protein expression when cultured in acetate/glutamine-only media, whereas shCon cells
242 maintained stable CAD levels (Fig. 3Q).
243
244 **ACSS1 supports growth under nutrient restriction**
245 We confirmed efficient ACSS1 knockdown (KD) in Maver and Jeko-1 cells using Western blot analysis,
246 with two of four shRNA clones achieving near-complete protein depletion (Fig. 4A). ACSS1 KD led to a
247 significant reduction in cell growth ($P < 0.0001$), as assessed by automated cell counting and trypan blue
248 exclusion (Fig. 4B). To assess the role of ACSS2, Jeko-1 and Maver cells were treated with an ACSS2
249 inhibitor (10–30 μM), resulting in a dose-dependent decrease in cell growth (Fig. 4C). Under metabolic
250 stress conditions, cells were cultured in glucose- and glutamine-free media supplemented with 1% dialyzed
251 FBS. While the viability of shCon and shACSS1 cells remained stable in complete media, ACSS1 KD cells

252 showed a marked decline in viability under nutrient deprivation. Supplementation with 100 μM acetate
253 significantly rescued viability in ACSS1 KD cells (from 16% to >68%) and in controls (from 36% to
254 >82%), highlighting ACSS1's critical role in acetate metabolism (Fig. 4D, E). Although glucose and
255 glutamine supplementation restored viability in control cells, glutamine was less effective in rescuing
256 ACSS1 KD cells. To determine whether impaired pyrimidine synthesis contributed to cell death, we
257 supplemented cultures with 100 μM uridine under nutrient-deprived conditions. Uridine markedly
258 enhanced viability in both control and ACSS1 KD cells ($P < 0.0001$; Fig. 4F, G). A schematic model (Fig.
259 4H) illustrates how ACSS1 overexpression promotes the generation of TCA cycle intermediates from
260 mitochondrial acetate, providing a critical carbon source that enhances nucleotide biosynthesis and
261 supports tumor growth. In contrast, ACSS1 knockdown cells (Fig. 5I) exhibit impaired production of
262 mitochondrial acetate-derived TCA cycle intermediates in the absence of acetate, leading to increased cell
263 death and reduced tumor burden. Notably, acetate supplementation rescues cell death in ACSS1-deficient
264 cells. This compensatory effect is mediated by upregulation of the cytosolic acetate-metabolizing enzyme
265 ACSS2, which converts acetate into acetyl-CoA, thereby increasing histone acetylation and promoting
266 transcription of pro-survival genes (Fig. 4J). Similarly, uridine supplementation partially rescues cell death
267 by supporting the pyrimidine salvage pathway. Uridine is directly converted to UMP by UCK1/2, restoring
268 nucleotide balance and sustaining cell proliferation and tumor growth. Importantly, this uridine-mediated
269 rescue occurs independently of TCA cycle intermediate restoration and does not involve alterations in
270 cytosolic acetate metabolism. Collectively, these findings demonstrate that ACSS1 sustains tumor growth
271 by supporting mitochondrial TCA cycle intermediates and pyrimidine precursor production, while also
272 revealing metabolic vulnerabilities that may be therapeutically exploited upon ACSS1 loss.
273
274
275
276

277 **ACSS1 Knockdown Reduces *In Vivo* Tumor Burden in Mantle Cell Lymphoma Models**

278 To evaluate whether ACSS1 promotes in vivo cancer growth during mantle cell lymphoma progression, we
279 used Luciferase-expressing JeKo-1 and Maver cells expressing control shRNA (shCon) or shRNA targeting
280 ACSS1 (shACSS1). These cells were injected into NSG mice, and tumor growth was monitored by
281 bioluminescence imaging (BLI). The BLI imaging of Jeko-1 shCon and shACSS1 injected mice is shown
282 (Fig.5A). Tumor burden was quantified as total photon flux (photons/sec) within defined regions of interest
283 (Fig.5B). In the JeKo-1 model, mice injected with shACSS1 cells demonstrated a significant reduction in
284 tumor burden compared with shCon controls at days 14 and 21 post-inoculation. BLI measurements
285 revealed a progressive divergence between groups, with the shACSS1 cohort consistently exhibiting lower
286 photon flux at these time points (Welch's two-sample t-test, two-tailed $p < 0.05$).

287 Similarly, in the Maverl, ACSS1 knockdown resulted in significantly reduced tumor burden at days 14 and
288 21 compared with shCon-injected mice. The reduction in photon flux in the shACSS1 group was consistent
289 across animals and remained statistically significant following adjustment for multiple comparisons using
290 the Holm–Bonferroni method (Fig. 5C, D). These findings demonstrate that ACSS1 suppression
291 significantly impairs in vivo tumor progression in both JeKo-1 and MAVER mantle cell lymphoma models.

292

293 **Discussion**

294 In this study, we identify ACSS1 as a key metabolic enzyme that enables mantle cell lymphoma (MCL)
295 cells to utilize acetate as a carbon source under nutrient-limited conditions. By integrating TCGA analysis,
296 ^{13}C-acetate isotope tracing metabolomics, and functional assays, we show that ACSS1 is highly expressed
297 in MCL and other hematological malignancies and contributes to metabolic flexibility by supporting
298 mitochondrial acetate metabolism, particularly when glucose and glutamine are scarce.

299 Our data show that MCL cell lines with high ACSS1 expression, such as Jeko-1 and Maver, demonstrate
300 increased incorporation of ^{13}C-acetate into TCA cycle intermediates, pyrimidine precursors, and
301 downstream nucleotides, compared to RL cells with low ACSS1 expression. This suggests a model in which
302 ACSS1 acts as a mitochondrial gatekeeper for acetate utilization, enabling continued energy production

303 and biosynthesis in adverse nutrient environments. These findings are in agreement with prior studies in
304 AML and melanoma models, where ACSS1 overexpression was linked to increased mitochondrial
305 incorporation of acetate-derived carbon into the TCA cycle(23).
306 Our immunohistochemical analysis of patient-derived tumor samples confirms that ACSS1 is frequently
307 expressed in MCL and DLBCL tissues, consistent with publicly available RNA-seq datasets from
308 hematologic and solid tumors. Notably, we observed heterogeneous ACSS1 expression within and across
309 lymphoma subtypes, suggesting metabolic diversity and differential reliance on acetate metabolism in the
310 tumor microenvironment. ACSS1 expression correlated with increased incorporation of ^{13}C-labeled acetate
311 into TCA cycle intermediates and pyrimidine pathway metabolites, highlighting its role in maintaining
312 biosynthetic capacity under conditions of glucose and glutamine deprivation.
313 Importantly, inhibiting ACSS1 impairs this metabolic flexibility. Our results show that knocking down
314 ACSS1 markedly decreases ^{13}C-acetate integration into TCA cycle intermediates, dihydroorotate, and
315 orotate, which results in reduced pyrimidine production and diminished cell viability when nutrients are
316 limited. These effects were partly restored by adding exogenous acetate or uridine, confirming that ACSS1
317 supports nucleotide synthesis through mitochondrial acetate metabolism. Additionally, oxygen
318 consumption rates (OCR) depend on ACSS1 expression, showing that acetate oxidation via ACSS1
319 contributes to mitochondrial respiration and energy generation. Overall, our results identify ACSS1 as a
320 key regulator of mitochondrial acetate metabolism in MCL. Unlike the better-understood cytosolic enzyme
321 ACSS2, which promotes lipid biosynthesis and histone acetylation(24-26). ACSS1 specifically directs
322 acetate into mitochondrial oxidative pathways and biosynthesis(14). In an earlier report, the role of
323 Mitochondrial ACSS1-K635 acetylation knock-in mice shows altered liver lipid metabolism on a ketogenic
324 diet(27). In another report, ACSS1-K635 acetylation knock-in mice exhibit altered metabolism, cellular
325 senescence, and nonalcoholic fatty liver disease(3). This highlights the significance of compartmentalized
326 acetate metabolism in helping cancer cells survive under metabolic stress.
327

328 Furthermore, our in vivo bioluminescence imaging confirmed that ACSS1-mediated acetate metabolism
329 regulates tumor burden in mantle cell lymphoma.
330 Metabolic reprogramming is a hallmark of mantle cell lymphoma (MCL), yet the role of mitochondrial
331 acetate metabolism in disease progression remains poorly defined. In this study, we demonstrate that
332 suppressing ACSS1 significantly impairs in vivo tumor growth in two independent MCL xenograft models.
333 Using luciferase-expressing JeKo-1 and MAVER cells, we show that ACSS1 knockdown results in a
334 marked and sustained reduction in tumor burden at days 14 and 21 post-engraftment, as measured by
335 longitudinal bioluminescence imaging (Fig. 5). The consistent attenuation of tumor growth across both
336 models supports a functional role for ACSS1 in promoting MCL progression in vivo. Reduced tumor
337 growth following ACSS1 suppression likely reflects impaired mitochondrial metabolism, limiting
338 nucleotide biosynthesis and proliferation under in vivo conditions. The delayed divergence in tumor burden
339 suggests that ACSS1 is particularly important as metabolic demand increases during tumor expansion.
340 These findings position ACSS1 as a potential metabolic vulnerability in MCL, distinct from cytosolic
341 ACSS2, and suggest that targeting mitochondrial acetate metabolism could impair tumor growth. Future
342 studies should clarify whether the effects of ACSS1 loss are mediated primarily through energy production,
343 nucleotide synthesis, or other biosynthetic pathways, and assess potential compensatory mechanisms.
344 Evaluating ACSS1 expression in primary MCL samples and its association with disease severity is also
345 important to establish its translational relevance. In summary, ACSS1 promotes MCL progression in vivo,
346 identifying mitochondrial acetate metabolism as a promising therapeutic target.
347
348 Therapeutically, these findings open new avenues for targeting metabolic dependencies in MCL. Inhibiting
349 acetate metabolism, either by directly inhibiting ACSS1 or by limiting acetate availability, may hinder
350 tumor cell survival, particularly in nutrient-poor microenvironments such as the tumor core or during
351 treatment-induced metabolic stress. Additionally, ACSS1 expression could serve as a biomarker to stratify
352 tumors by their dependence on mitochondrial acetate metabolism. Our results also suggest therapeutic

353 implications. Tumors with high ACSS1 expression may be selectively vulnerable to strategies that disrupt
354 acetate metabolism or target downstream biosynthetic pathways, such as pyrimidine synthesis.
355 In summary, we provide evidence that ACSS1-driven acetate utilization supports pyrimidine biosynthesis
356 and cell survival under metabolic stress in MCL cells. These findings advance our understanding of
357 metabolic plasticity in lymphoid malignancies and highlight ACSS1 as a potential metabolic vulnerability
358 with therapeutic relevance.
359

360 **Materials and Methods**

361 ACSS1 (Cat#17138-1-AP,RRID:AB_2289182), ACLY (Cat# 67166-1-Ig; RRID:AB_2882462), GAPDH
362 (Cat# 60004-1-Ig;RRID:AB_2107436), DHODH (Cat# 14877-1-AP, RRID:AB_2091723), CAD (Cat#
363 16617-1-AP, RRID:AB_2878289) and VDAC1 (Cat# 66345-1-Ig, RRID:AB_2881725) from Proteintech
364 Inc., ACSS2 (Cat#3658S; RRID:AB_2222710) from Cell Signaling Technology. ^{13}C2-Sodium acetate
365 (Cat#CLM-440-1) from Cambridge Isotope Laboratories. The special media, D-Glucose-free RPMI 1640
366 (REF 11879-020), was obtained from Gibco. RPMI 1640 (-) Glutamine free and (-) D-Glucose free media
367 were obtained from BI, Biological Industries, Israel Beit-Haemek. Uridine (Sigma, catalog#U3750-1G).
368

369 **MCL and DLBCL cell lines**

370 Cell lines from different lymphomas were used, including MCL-RL(28), a cell line derived from a patient
371 with MCL at the University of Pennsylvania, Philadelphia, PA, JeKo-1, Maver, Rec-1, and Granta519 for
372 MCL; OCI-LY1, OCI-LY4, OCI-LY8, and TOLEDO for DLBCL; All commercially available cell lines
373 were obtained from the American Type Culture Collection (ATCC). All the cell lines were regularly tested
374 for Mycoplasma contamination using Mycoplasma detection kits from Thermo Fisher Scientific and
375 authenticated. All cells were grown in RPMI medium supplemented with 10% FBS and 1%
376 penicillin/streptomycin under a humidified 37°C/5% CO_2 incubator. The cell lines are validated for
377 authenticity and routinely tested for mycoplasma contamination.

378 **Nutrient starvation in cell culture**

379 For nutrient-deprivation experiments, cells were washed once with phosphate-buffered saline. The
380 glutamine-free medium was made with RPMI devoid of glutamine and glucose and retained the same
381 nutrient concentrations as standard RPMI with dialyzed 10% FBS and 25 mM Glucose. A glucose-free
382 medium was made with RPMI devoid of glutamine and glucose and retained the same nutrient
383 concentrations as standard RPMI with dialyzed 10% FBS and 2 mM Glutamine. Complete RPMI was
384 prepared by supplementing with 2 mM L-Glutamine and 25 mM Glucose to RPMI devoid of glutamine and
385 glucose. For acetate supplementation, Sodium acetate at a final concentration of 5 mM was supplemented
386 to Glutamine-free or Glucose-free media or both Glutamine/Glucose-free media.

387 **ACSS1 and mitochondrial fractionation**

388 For mitochondria isolation, $50x10^6$ cells of Jeko-1 and Maver cell lines were harvested, and mitochondria
389 were isolated according to the instructions of the product manual (catalog # 89874, Thermofisher). The
390 protein estimation was measured, and an equal amount of protein was separated on a 10% NuPAGE gel
391 and processed for western blotting as described below.

392 **ACSS1 knockdown (KD) in MCL cell lines**

393 Jeko-1 and Maver cell lines were transduced with the scramble PLKO.1-PURO NON-TARGET
394 CONTROL (SHC016V-1EA) and ACSS1 shRNA, TRCN0000436733, TRCN0000045380,
395 TRCN0000045381, TRCN0000424197 and TRCN0000423168 all purchased from Millepore-Sigma-
396 Aldrich. The ready-to-transduce lentivirus particles were directly mixed with 100,000 cells (Jeko-1 and
397 Maver) in the presence of polybrene (catalog#TR-1003-G, Millepore Sigma) in a 96-well plate. The media
398 was replaced with fresh RPMI after 16 hours of incubation. The cells were cultured for an additional 3 days
399 and then selected with puromycin.

400 **In Vivo Bioluminescence Imaging**

401 For in vivo bioluminescence imaging (BLI) studies, JeKo-1 and MAVER mantle cell lymphoma cell lines
402 stably expressing either control shRNA (shCon) or shRNA targeting ACSS1 (shACSS1) were transduced
403 in vitro with the Click Beetle Green luciferase reporter prior to inoculation to enable longitudinal tumor

404 monitoring. For the JeKo-1 model, 0.7×10^6 cells (shCon or shACSS1) were injected per mouse. For the
405 MAVER model, 1.6×10^6 shCon cells or 1.8×10^6 shACSS1 cells were injected per mouse. Cells were
406 administered via lateral tail vein injection into NSG mice. Tumor burden was quantified by measuring total
407 photon flux (photons/sec) within predefined regions of interest (ROIs). Bioluminescence signals were
408 collected longitudinally and used to assess tumor progression for each animal. Group means and standard
409 errors of the mean (SEM) were calculated from individual animal measurements using standard
410 propagation-of-error formulas. Statistical comparisons between groups were performed using Welch's two-
411 sample t-test applied to per-animal values. All tests were two-tailed. When multiple comparisons were
412 conducted, p-values were adjusted using the Holm–Bonferroni method.
413
414 **Western blotting**
415 Cells were harvested and processed for western blotting as previously described with respective antibodies;
416 blots were developed using the Ibright 1500 imaging system (Thermo Scientific)(29).
417 **Reverse transcription quantitative polymerase chain reaction**
418 MCL-RL, Jeko-1, and Maver, along with Jeko-1 shCon or shACSS1 cells, were seeded in six-well plates
419 up to 48 hours. RNA isolation and DNase treatment were performed according to the kit protocol (Qiagen
420 #74104, #79254). The RNA concentration was measured, and 1 µg was used for cDNA synthesis, which
421 was performed with SuperScript IV (Invitrogen #18091050). For the quantitative reverse transcription
422 polymerase chain reaction (qRT-PCR), 1 µL of cDNA was utilized. Each reaction contained: 1 µL of cDNA,
423 5 µL of SYBR Green mix (Applied Biosystem, A25742), 0.5 µL of forward primer (from a 10 mM stock),
424 0.5 µL of reverse primer (from a 10 mM stock), and 3 µL of dH2O. Each condition was tested in technical
425 triplicate. Primers used are as follows,
426 **Primer Sequence 5' to 3'**
427 ACSS1, Forward- TTG AGA GCA CCC CAG TTT ATC; Reverse- GCA TCA CCG TAT TTC AGC AAC
428 ACSS2, Forward- GGA TCA CTG GTC ATT CCT AC; Reverse- GTG CTG TGT AGA ACT TGG TC

429 CAD, Forward- AGT GGT GTT TCA AAC CGG CAT; Reverse- CAG AGG ATA GGT GAG CAC TAA
430 GA and DHODH, Forward-CCACGGGAGATGAGCGTTTC; Reverse-CAGGGAGGTGAAGCGAACA

431 **Immunohistochemistry (IHC) of MCL, DLBCL, and CLL patient-derived biopsy samples.**

432 We followed the protocols approved by the Institutional Review Board (IRB) of Fox Chase Cancer Center.
433 Frozen DLBCL and MCL patient tissue samples were isolated from IRB-exempt discarded specimens of
434 patients with diffuse large B-cell lymphoma (DLBCL) obtained through the Fox Chase Cancer Center Bio
435 Specimen Repository. Human tissue microarrays for patients with MCL ($n = 22$), DLBCL ($n = 28$) and CLL
436 (n=7) were used to examine ACSS1. The expression of ACSS1 was analyzed according to the pathology
437 grade of the samples. Tissues were collected and fixed in 10% phosphate-buffered formaldehyde (formalin)
438 for 24-48 hrs, dehydrated and embedded in paraffin. Hematoxylin and eosin (H&E) stained sections were
439 used for morphological evaluation and unstained sections for IHC studies. IHC staining was performed on
440 a VENTANA Discovery XT automated staining instrument (Ventana Medical Systems) using VENTANA
441 reagents according to the manufacturer's instructions. Slides were de-paraffinized using EZ Prep solution
442 (cat # 950–102) for 16 min at 72 °C. Epitope retrieval was accomplished with CC1 solution (cat # 950–
443 224) at high temperature (eg, 95–100 °C) for 32 min. Rabbit primary antibodies (ACSS1: 1:200, ACSS1
444 (Cat#17138-1-AP, RRID :AB_2289182) were tittered with a TBS antibody diluent into user-fillable
445 dispensers for use on the automated stainer. Immune complex was detected using the Ventana OmniMap
446 anti-rabbit detection kit (760-4311) and developed using the VENTANA ChromMap DAB detection kit
447 (cat # 760-159) according to the manufacturer’s instructions. Slides were then counterstained with
448 hematoxylin II (cat # 790-2208) for 8 min, followed by Bluing reagent (cat # 760-2037) for 4 min. The
449 slides were dehydrated with ethanol series, cleared in xylene, and mounted. As a negative control, the
450 primary antibody was replaced with normal rabbit IgG to confirm the absence of specific staining. Stained
451 slides were scanned using an Aperio ScanScope CS 5 slide scanner (Aperio, Vista, CA, USA). Scanned
452 images were then viewed and captured with Aperio's image viewer software (ImageScope, version
453 11.1.2.760, Aperio).

454 **Cell proliferation and cell death analysis**

455 For measuring cell proliferation, MCL Jeko-1 and Maver parental cell lines were seeded at a density of 2 ×
456 10^4 cells per well in 96-well plates (Corning, NY, USA). Afterwards, the cells were treated with different
457 concentrations of the ACSS2 inhibitor and incubated for 72 hours. After incubation, the cells were counted
458 using the trypan blue method with a hemocytometer.

459 **Cell Culture Conditions under Nutrient Deprivation**

460 Jeko-1 and Maver lymphoma cell lines shCon and shACSS1 were cultured under various nutrient
461 conditions to assess the role of ACSS1 in supporting cell viability during metabolic stress.
462 Cells were seeded at a density of 2×10^5 cells/mL and cultured for 72 hours under the following conditions:
463 Complete RPMI medium supplemented with 10% FBS, Glucose- and glutamine-free RPMI supplemented
464 with 1% dialyzed FBS, Glucose- and glutamine-free RPMI supplemented with 1% dialyzed FBS and 1 mM
465 sodium acetate, Glucose- and glutamine-free RPMI supplemented with 1% dialyzed FBS and 2 mM
466 glucose, and Glucose- and glutamine-free RPMI supplemented with 1% dialyzed FBS and 2 mM glutamine
467 For pyrimidine depletion and rescue experiments, shACSS1 and shCon cells were cultured in glucose- and
468 glutamine-free RPMI supplemented with 1% dialyzed FBS, in the presence or absence of 100 μM uridine
469 (Cat# U3750-1G, Sigma-Aldrich), a pyrimidine nucleoside metabolite.
470 Following incubation, cell viability was assessed using the protocol as described in the kit for Annexin V /
471 Propidium Iodide (PI) Staining ((BD Biosciences Cat# 556547, RRID:AB_2869082BD) and flow
472 cytometry for cell viability assay.
473

474 **Metabolomics analysis**

475 Metabolomics analyses were conducted at The Wistar Institute Proteomics and Metabolomics Shared
476 Resource with slight modifications as previously described(30). For $^{13}C_2$-acetate tracing experiments, the
477 cells were cultured in glucose- and glutamine-free RPMI-1640 media supplemented with 500 μM labeled
478 $^{13}C_2$-acetate (Cambridge Isotope Laboratories Inc.), 10 mM unlabeled Glucose for 16 hours in triplicate.
479 The cells were counted using the trypan blue method, and an equal number of cells ($10x10^6$ cells/condition)

480 were spun down at 1,000 rpm for 5 minutes. The cell pellet was washed with cold PBS and snap-frozen in
481 liquid nitrogen. Unlabeled controls were generated for each cell line condition.

482 **Oxygen consumption rate (OCR) measurement by Seahorse analysis.**

483 The MCL cell lines (Jeko-1 shControl (control), Jeko-1 shACSS1 knockdown (KD), Maver shControl
484 (control), Maver shACSS1 knockdown (KD) were exposed to either -glucose (Glc) or 2 mM acetate (ACE)
485 for 1 hour and then thoroughly examined for mitochondrial respiration using the Seahorse-based method.
486 The XF Mitochondrial stress test kit protocols (Agilent) were followed using the Agilent Seahorse XFe96
487 analyzer per the manufacturer's instructions. In brief, cells were seeded in Seahorse XF 96-well plates at a
488 density of 1.2x 10^5 cells per well with Assay Base media, supplemented with 10 mM Glucose, 1 mM
489 Sodium Pyruvate, and 2 mM Glutamine. The cell cultures were allowed to equilibrate for 1 hour at 37 °C
490 in a no-CO2 incubator. The Oxygen Consumption Rate was analyzed under basal conditions and after
491 treatment with different drugs, including 1 μM oligomycin A, 2 μM FCCP, and 0.5 μM Rot/AA. After the
492 analysis, the medium was removed, and the cells were suspended in RIPA lysis buffer. The protein content
493 of the cell lysates was then measured using the Bradford assay and used to normalize the respiratory
494 parameters. Samples were analyzed with at least 6 technical replicates. The data were assessed using XF
495 Wave Software (Seahorse Bioscience, Agilent).

496 **Statistics and reproducibility**

497 The student's unpaired t-test was used to analyze differences in quantitative (q)-PCR expression analysis,
498 and isotope-labeled metabolites compared with MCL-RL cell line vs. Jeko-1 and Maver in three ^{13}C-isotope
499 tracing experiments. For ACSS1 knockdown (KD) studies in Jeko-1 and Maver cell lines, an unpaired t-
500 test was used to analyze differences between control vs. KD cells ^{13}C-acetate isotope-labeled metabolites.
501 The student's t-test was used to analyze differences in metabolites. p-values equal to or less than 0.05 were
502 considered statistically significant without being adjusted for multiple comparisons. The statistical analysis
503 was performed using GraphPad Prism 9.0. software.

504 Data availability

We confirm that all relevant data and methods are included in the main Article and the Supplementary Information section.

References

1. Hosios AM, Hecht VC, Danai LV, Johnson MO, Rathmell JC, Steinhauser ML, et al. Amino Acids Rather than Glucose Account for the Majority of Cell Mass in Proliferating Mammalian Cells. Dev Cell. 2016;36(5):540-9.
2. Schug ZT, Vande Voorde J, Gottlieb E. The metabolic fate of acetate in cancer. Nat Rev Cancer. 2016;16(11):708-17.
3. Xu G, Quan S, Schell J, Gao Y, Varmazyad M, Sreenivas P, et al. Mitochondrial ACSS1-K635 acetylation knock-in mice exhibit altered metabolism, cell senescence, and nonalcoholic fatty liver disease. Sci Adv. 2024;10(20):eadj5942.
4. Wang J, Yang Y, Shao F, Meng Y, Guo D, He J, et al. Acetate reprogrammes tumour metabolism and promotes PD-L1 expression and immune evasion by upregulating c-Myc. Nat Metab. 2024.
5. Schwer B, Bunkenborg J, Verdin RO, Andersen JS, Verdin E. Reversible lysine acetylation controls the activity of the mitochondrial enzyme acetyl-CoA synthetase 2. P Natl Acad Sci USA. 2006;103(27):10224-9.
6. Berg P. Acyl adenylates; an enzymatic mechanism of acetate activation. J Biol Chem. 1956;222(2):991-1013.
7. Comerford SA, Huang Z, Du X, Wang Y, Cai L, Witkiewicz AK, et al. Acetate dependence of tumors. Cell. 2014;159(7):1591-602.
8. Bulusu V, Tumanov S, Michalopoulou E, van den Broek NJ, MacKay G, Nixon C, et al. Acetate Recapturing by Nuclear Acetyl-CoA Synthetase 2 Prevents Loss of Histone Acetylation during Oxygen and Serum Limitation. Cell Rep. 2017;18(3):647-58.
9. Wellen KE, Thompson CB. A two-way street: reciprocal regulation of metabolism and signalling. Nat Rev Mol Cell Bio. 2012;13(4):270-U1.
10. Watkins PA, Maiguel D, Jia ZZ, Pevsner J. Evidence for 26 distinct acyl-coenzyme A synthetase genes in the human genome. J Lipid Res. 2007;48(12):2736-50.
11. Murthy D, Attri KS, Shukla SK, Thakur R, Chaika NV, He CB, et al. Cancer-associated fibroblast-derived acetate promotes pancreatic cancer development by altering polyamine metabolism via the ACSS2-SP1-SAT1 axis. Nat Cell Biol. 2024.
12. Yun M, Bang SH, Kim JW, Park JY, Kim KS, Lee JD. The importance of acetyl coenzyme A synthetase for 11C-acetate uptake and cell survival in hepatocellular carcinoma. J Nucl Med. 2009;50(8):1222-8.
13. Comerford SA, Huang Z, Du X, Wang Y, Cai L, Witkiewicz AK, et al. Acetate Dependence of Tumors. Cell. 2014;159(7):1591-602.
14. Mashimo T, Pichumani K, Vemireddy V, Hatanpaa KJ, Singh DK, Sirasanagandla S, et al. Acetate Is a Bioenergetic Substrate for Human Glioblastoma and Brain Metastases. Cell. 2014;159(7):1603-14.
15. Schug ZT, Peck B, Jones DT, Zhang QF, Grosskurth S, Alam IS, et al. Acetyl-CoA Synthetase 2 Promotes Acetate Utilization and Maintains Cancer Cell Growth under Metabolic Stress. Cancer Cell. 2015;27(1):57-71.
16. Lee MY, Yeon A, Shahid M, Cho E, Sairam V, Figlin R, et al. Reprogrammed lipid metabolism in bladder cancer with cisplatin resistance. Oncotarget. 2018;9(17):13231-43.

549 17. Li CJ, Chiu YH, Chang C, Chang YCI, Sheu JJC, Chiang AJ. Acetyl Coenzyme A Synthase 2 Acts as a
550 Prognostic Biomarker Associated with Immune Infiltration in Cervical Squamous Cell Carcinoma.
551 Cancers. 2021;13(13).
552 18. Sakakibara I, Fujino T, Ishii M, Tanaka T, Shimosawa T, Miura S, et al. Fasting-induced
553 Hypothermia and Reduced Energy Production in Mice Lacking Acetyl-CoA Synthetase 2. Cell Metab.
554 2009;9(2):191-202.
555 19. Calhoun S, Duan L, Maki CG. Acetyl-CoA synthetases ACSS1 and ACSS2 are 4-hydroxytamoxifen
556 responsive factors that promote survival in tamoxifen treated and estrogen deprived cells. Transl Oncol.
557 2022;19.
558 20. Aitken SC, Lippman ME. Hormonal-Regulation of De Novo Pyrimidine Synthesis and Utilization in
559 Human-Breast Cancer-Cells in Tissue-Culture. Cancer Res. 1983;43(10):4681-90.
560 21. Kamphorst JJ, Chung MK, Fan J, Rabinowitz JD. Quantitative analysis of acetyl-CoA production in
561 hypoxic cancer cells reveals substantial contribution from acetate. Cancer Metab. 2014;2:23.
562 22. Monga N, Tam C, Garside J, Davids MS, Ward K, Quigley J, et al. Clinical efficacy and safety of
563 first-line treatments in patients with mantle cell lymphoma: A systematic literature review. Crit Rev
564 Oncol Hematol. 2021;158:103212.
565 23. Hlavaty SI, Salcido KN, Pniewski KA, Mukha D, Ma W, Kannan T, et al. ACSS1-dependent acetate
566 utilization rewires mitochondrial metabolism to support AML and melanoma tumor growth and
567 metastasis. Cell Rep. 2024;43(12):114988.
568 24. Mews P, Donahue G, Drake AM, Luczak V, Abel T, Berger SL. Acetyl-CoA synthetase regulates
569 histone acetylation and hippocampal memory. Nature. 2017;546(7658):381-6.
570 25. Hu W, Wang X, Fang Z, Zhang J, Tirumalasetty MB, Miao QR. High fructose promotes MYCN-
571 amplified neuroblastoma progression through NgBR-ACSS2-mediated biosynthesis of acetyl-CoA. Cell
572 Rep. 2025;44(7):115947.
573 26. Zhang Y, He S, Wang X, Wang X, He MY, Yu XX, et al. ACSS2 mediates an epigenetic pathway to
574 regulate beta-cell adaptation during gestation in mice. Nat Commun. 2025;16(1):4697.
575 27. Xu G, Schell J, Quan S, Gao Y, Wei SJ, Pan M, et al. Mitochondrial ACSS1-K635 acetylation knock-
576 in mice exhibit altered liver lipid metabolism on a ketogenic diet. Free Radic Biol Med. 2025;232:260-8.
577 28. Lee SC, Shestov AA, Guo LL, Zhang Q, Roman JC, Liu XB, et al. Metabolic Detection of Bruton's
578 Tyrosine Kinase Inhibition in Mantle Cell Lymphoma Cells. Molecular Cancer Research. 2019;17(6):1365-
579 77.
580 29. Basappa J, Citir M, Zhang Q, Wang HY, Liu XB, Melnikov O, et al. ACLY is the novel signaling
581 target of PIP/PIPand Lyn in acute myeloid leukemia. Heliyon. 2020;6(5).

582 30. Di Marcantonio D, Martinez E, Kanefsky JS, Huhn JM, Gabbasov R, Gupta A, et al. ATF3
583 coordinates serine and nucleotide metabolism to drive cell cycle progression in acute myeloid leukemia.
584 Mol Cell. 2021;81(13):2752-+.

585

586 **Acknowledgments**

587 We are grateful to Dr. Erica Golemis, Senior Associate Dean of Research at Lewis Katz School of Medicine,
588 Temple University Health System, and Professor and Chair, Cancer and Cellular Biology, Fox Chase
589 Cancer Center, Philadelphia, for critically reading the manuscript and providing feedback to improve the
590 paper. We thank the IHC core facility members at Fox Chase Cancer Center for providing excellent IHC

staining. We thank Dr. Andrey Efimov, Bio Imaging Facility, Fox Chase Cancer Center, for confocal imaging. We created the figures in this manuscript using the Biorender program..

Funding:

The funding for the startup comes from Fox Chase Cancer Center to MW. The Wistar Institute Proteomics and Metabolomics Shared Resource is supported by NIH Cancer Center Support Grant CA010815. The metabolomics analysis was performed on a Thermo Q-Exactive HF-X mass spectrometer purchased with NIH grant S10 OD023586.

Author Contributions:

Conceptualization: J.B. Writing original draft: J.B. Data curation: J.B. Methodology: J.B., A.R.G. and N.V.S. Formal Analysis: J.B., A.R.G., and D.R. Investigation: J.B., C.L., S.W., D.R., O.M., N.V.S., V.S.M., P.J., M.E., R.N., K.Q.C., D.S.N., P.K.G., and K.N. Visualization: J.B., A.R.G., and C.L. Validation: J.B., A.R., D.R. and N.V.S. Resources: H.B., and K.E.W. Supervision: J.B. Writing, review and editing: J.B., A.R.G, C.L., K.E.W. and M.A.W. Funding acquisition: M.A.W. Read and approved of the manuscript: J.B., A.R.G., C.L., S.W., D.R., O.M., N.V.S., V.S.M., P.J., M.E., K.C., P.L., R.N., H.G., K.E.W., and M.A.W.

Competing interests

All authors declare that they have no competing interests.

Data and materials availability: All data needed to evaluate the conclusions in the paper are present in the paper and/or the Supplementary Materials.

Table of Contents

Main Fig. 1-5

Supplementary Fig. 1-4

Table 1

ACSS1 expression profile in the TCGA database across cancer models

618 **Fig. 1**

619 **ACSS1 expression shows variable expressions in MCL and DLBCL samples.**

620 **A,** Representative immunohistochemistry (IHC) images of ACSS1 protein expression in mantle cell
621 lymphoma (MCL) tissue microarray (TMA) cores, showing examples of strong, moderate, and weak
622 staining.

623 **B**, Quantification of ACSS1 IHC staining intensity in MCL (n = 27) samples. Staining intensity was
624 categorized as strong, moderate, weak, or negative.

625 **C,** Representative IHC images of ACSS1 expression in DLBCL TMA cores, corresponding to varying
626 expression levels.

627 **D,** Quantification of ACSS1 IHC staining intensity in diffuse large B-cell lymphoma (DLBCL, n = 44)
628 samples. Staining intensity was categorized as strong, moderate, weak, or negative.

629

630 Fig. 2

631 **Acetate feeds the TCA cycle in MCL and DLBCL cells in an ACSS1-dependent manner.**

632 **A-D**, Quantitative RT-PCR analysis of ACSS1 and ACSS2 mRNA expression in MCL (RL, Jeko-1, Maver)
633 and DLBCL (OCI-LY1, OCI-LY8) cell lines. ACSS1 is highly expressed in Jeko-1, Maver, and OCI-LY8,
634 while ACSS2 remains uniformly low.

635 **E, F**, Immunoblot analysis of ACSS1 protein levels across five MCL (e) and four DLBCL (f) cell lines
636 confirms elevated expression in all except RL and OCI-LY1, respectively. **G,** A schematic of ^{13}C-acetate
637 isotope tracing.

638 **H, I,** ^{13}C-acetate isotope tracing and LC-MS analysis of TCA cycle intermediates in RL, Jeko-1, and Maver
639 cells. unalabeled and labeled acetyl-CoA (**H**), M+0 to M+n isotopologues of citrate (**I**), α-ketoglutarate (**J**),
640 succinate (**K**), and malate (**L**) are enriched in ACSS1-high lines.

641 **M, N**, ACSS1 knockdown efficiency confirmed by qPCR and immunoblotting in Jeko-1 and Maver cells.
642 **O**, Schematic of isotope tracing strategy using ^{13}C-acetate in glucose- and glutamine-deprived media.

643 **P, Q**, ACSS1 knockdown reduces ^{13}C-acetate derived labeling of acetyl-CoA (**P**) and mitochondrial
644 acetylcarnitine (**Q**), confirming ACSS1's role in mitochondrial acetate conversion.

645 **R–U**, Stable isotope tracing reveals significantly decreased ^{13}C incorporation into citrate (**R**), aconitate (**S**),
646 α-ketoglutarate (**T**), and malate (**U**) upon ACSS1 silencing. **V**, Basal oxygen consumption rate (OCR)
647 increases in ACSS1-high Jeko-1 and Maver cells after acetate supplementation; no effect in low-ACSS1
648 RL cells.

649 **W, X**, ACSS1 knockdown reduces basal and stress-induced OCR in Jeko-1 (u) and Maver (v) cells under
650 acetate-reliant conditions.

651 All graphs show mean ± SD (n = 3 biological replicates), and all statistical analyses were conducted with
652 unpaired t-tests: $^{*}p < 0.05$, $^{**}p < 0.01$, $^{***}p < 0.001$, $^{****}p < 0.0001$

653 Fig.3

ACSS1 supports pyrimidine metabolism.

A, Schematic illustrating ^{13}C-acetate tracing strategy to assess incorporation into TCA cycle intermediates and downstream pyrimidine biosynthesis.

B, C, Mass isotopologue distribution analysis of aspartate (**B**) and glutamate (**C**) in RL (low ACSS1), Jeko-1, and Maver (high ACSS1) MCL cell lines shows significantly increased ^{13}C-labeling in ACSS1-high cells under nutrient-limited conditions (RPMI lacking glucose/glutamine, supplemented with ^{13}C-acetate).

D–G, Enhanced incorporation of ^{13}C into pyrimidine intermediates orotate (**D**), UMP (**E**), UDP (**F**), and CDP (**G**) in Jeko-1 and Maver compared to RL cells, indicating acetate contribution to de novo pyrimidine synthesis.

H, I, Knockdown of ACSS1 via shRNA (shACSS1) in Jeko-1 and Maver cells reduces ^{13}C-labeling of aspartate (**H**) and glutamate (**I**) compared to scramble controls (shCon).

J, K, ^{13}C-labeling of dihydroorotate (**J**) and orotate (**K**) is also significantly decreased in shACSS1 cells, confirming impaired pyrimidine biosynthesis.

L, Heat map highlighting significantly altered pyrimidine-related metabolites in Jeko-1 shACSS1 vs. shCon cells (fold change >1.5, $P < 0.05$).

M, N, Metabolite enrichment and pathway analysis of 206 profiled metabolites in shACSS1 cells reveals prominent suppression of the pyrimidine synthesis pathway.

O, Schematic of pyrimidine biosynthesis pathway showing ACSS1's proposed role and key enzymes (CAD, DHODH).

P, qRT-PCR analysis of CAD and DHODH mRNA levels shows reduced expression in shACSS1 cells.

Q, Western blot analysis reveals decreased CAD protein expression in shACSS1 cells cultured in acetate/glutamine-only media, supporting a regulatory role of ACSS1 in pyrimidine biosynthetic enzyme expression under metabolic stress.

All graphs show mean ± SD (n = 3 biological replicates), and all statistical analyses were conducted with unpaired t-tests: $^{*}p < 0.05$, $^{**}p < 0.01$, $^{***}p < 0.001$, $^{****}p < 0.0001$.

Fig. 4

ACSS1 supports growth under nutrient restriction.

A, Western blot analysis confirming efficient knockdown of ACSS1 in Maver and Jeko-1 cells using four independent shRNA clones; two clones exhibited near-complete protein depletion.

B, ACSS1 knockdown (KD) significantly reduced cell growth, assessed by automated cell counting and trypan blue exclusion over 72 hours ($P < 0.0001$).

C, Dose-dependent inhibition of cell growth by ACSS2 inhibitor (10–30 μM) in Jeko-1 and Maver cells cultured under standard conditions.

D, E, Cell viability under metabolic stress (glucose/glutamine-free media + 1% dialyzed FBS) was markedly reduced in shACSS1 cells compared to shCon. Supplementation with 100 μM acetate significantly rescued viability in both groups, with a more pronounced effect in ACSS1 KD cells.

691 **F, G**, Supplementation with 100 μM uridine rescued viability in both control and ACSS1 KD cells under
692 nutrient-deprived conditions ($P < 0.0001$), implicating impaired pyrimidine biosynthesis in reduced cell
693 survival.

694 **H.** Schematic model illustrating ACSS1-mediated conversion of acetate to mitochondrial acetyl-CoA,
695 fueling the TCA cycle and promoting the production of aspartate and glutamate to support de novo
696 pyrimidine biosynthesis. The model highlights the metabolic advantage conferred by ACSS1
697 overexpression in sustaining nucleotide synthesis and tumor growth.

698 **I.** Schematic model depicting impaired conversion of acetate to mitochondrial acetyl-CoA in ACSS1
699 knockdown cells. Reduced mitochondrial acetyl-CoA availability attenuates TCA cycle activity, leading
700 to diminished production of aspartate and glutamate and consequent suppression of pyrimidine
701 biosynthesis.

702 **J.** Schematic model showing partial rescue of ACSS1-deficient cells. Acetate supplementation enhances
703 compensatory ACSS2 activity in the cytosol, increasing acetyl-CoA production and histone acetylation to
704 promote transcription of pro-survival genes. Uridine supplementation independently restores nucleotide
705 balance by directly supporting UMP synthesis through the pyrimidine salvage pathway, thereby
706 sustaining nucleotide production under ACSS1-depleted conditions.

707 **Fig. 5**

708 **ACSS1 knockdown reduces tumor burden *in-vivo* in mantle cell lymphoma xenograft models.**
709 **A**. Representative bioluminescence imaging (BLI) of NSG mice injected with luciferase-expressing JeKo-
710 1 cells transduced with control shRNA (shCon) or ACSS1-targeting shRNA (shACSS1). Tumor growth
711 was monitored longitudinally by BLI.
712 **B**. Quantification of tumor burden in the JeKo-1 model expressed as total photon flux (photons/sec)
713 within defined regions of interest. Mice injected with shACSS1 cells exhibited significantly reduced
714 tumor burden compared with shCon controls at days 14 and 21 post-inoculation (Welch's two-sample t-
715 test, two-tailed, $p < 0.05$).
716 **C**. Representative BLI images of NSG mice injected with luciferase-expressing MAVER cells expressing
717 shCon or shACSS1.
718 **D**. Quantification of tumor burden in the MAVER model showing significantly reduced photon flux in
719 the shACSS1 group at days 14 and 21 post-inoculation. Statistical significance was maintained after
720 adjustment for multiple comparisons using the Holm–Bonferroni method.

721

722 Supplementary Fig.1

723 **Overview of tissue microarrays (TMAs) and ACSS1 expression in lymphoma**.

724 **A**, Low-magnification overview of the mantle cell lymphoma (MCL) TMA block used for
725 immunohistochemical analysis of ACSS1 expression.

726 **B**, Representative IHC images showing ACSS1 staining in diffuse large B-cell lymphoma (DLBCL)
727 patient samples (n = 13). ACSS1 expression was detected in 7 cases (53.8%).

728

729 Supplementary Fig.2

730 **Validation of ACSS1 antibody specificity and mitochondrial localization**.

731 **A, B**, Immunofluorescence analysis of a breast cancer tissue section stained with antibodies against
732 ACSS1 (green) and the mitochondrial marker VDAC1 (red), with nuclei counterstained using DAPI
733 (blue). Confocal microscopy shows co-localization of ACSS1 and VDAC1 in positive control tissue.

734 **C**, Negative control showing absence of ACSS1 signal in breast cancer tissue, confirming antibody
735 specificity.

736 **D**, Subcellular fractionation and immunoblot analysis of MCL cell lines (Maver and Jeko-1) demonstrate
737 enrichment of ACSS1 in mitochondrial fractions. VDAC1 serves as a mitochondrial marker.

738

739 Supplementary Fig.3

740 **ACSS1 is selectively expressed in non-Hodgkin lymphoma models**.

741 **A**, RNA-seq–based expression analysis of acetyl-CoA synthetase family members (ACSS1, ACSS2,
742 ACSS3) across hematological cancer cell lines using the Expression Atlas database. Data includes models
743 of mantle cell lymphoma (MCL), diffuse large B-cell lymphoma (DLBCL), chronic lymphocytic
744 leukemia (CLL), acute myeloid leukemia (AML), and anaplastic large cell lymphoma (ALCL).

745 **B**, ACSS1 expression is elevated in non-Hodgkin lymphoma (NHL) cell lines and patient-derived
746 samples, whereas ACSS3 expression is consistently low or undetectable (FPKM <1) across all profiles.

747 Supplementary Fig. 4 |

748 **ACSS1 knockdown alters pyrimidine-associated metabolites under acetate-reliant conditions.**

749 **A, B,** Heatmap analysis of metabolomic profiling of shACSS1 and shControl Jeko-1 and Maver cells
750 cultured in glucose- and glutamine-free media supplemented with 1% dialyzed FBS and ^{13}C-acetate. Of
751 the 206 metabolites analyzed, 46 showed significant changes (fold change >1.5, $P < 0.05$), with a majority
752 enriched in the pyrimidine biosynthesis pathway. Data represents results from two independent cell lines
753 (Jeko-1 and Maver), each with triplicate biological replicates.

754

755 **Table 1**

756 **ACSS1**

757 ACSS1 expression profile in the TCGA database across cancer models

758

759

760

Cancer type	Total number of samples tested	No. of samples over expressed	Over expressed (%)	No. of samples under expressed	Under expressed (%)
Hematologic and lymphoid	221	80	36.2	3	1.36
Central Nervous System	697	557	79.91	32	4.59
Lung	1019	111	10.89	None	None
Ovary	266	78	29.32	None	None
Cervix	307	258	84.04	29	9.45
Large Intestine	610	158	25.9	12	1.97
Prostate	498	82	16.47	3	0.6
Head and Neck	522	129	24.71	None	None

761

Fig.1

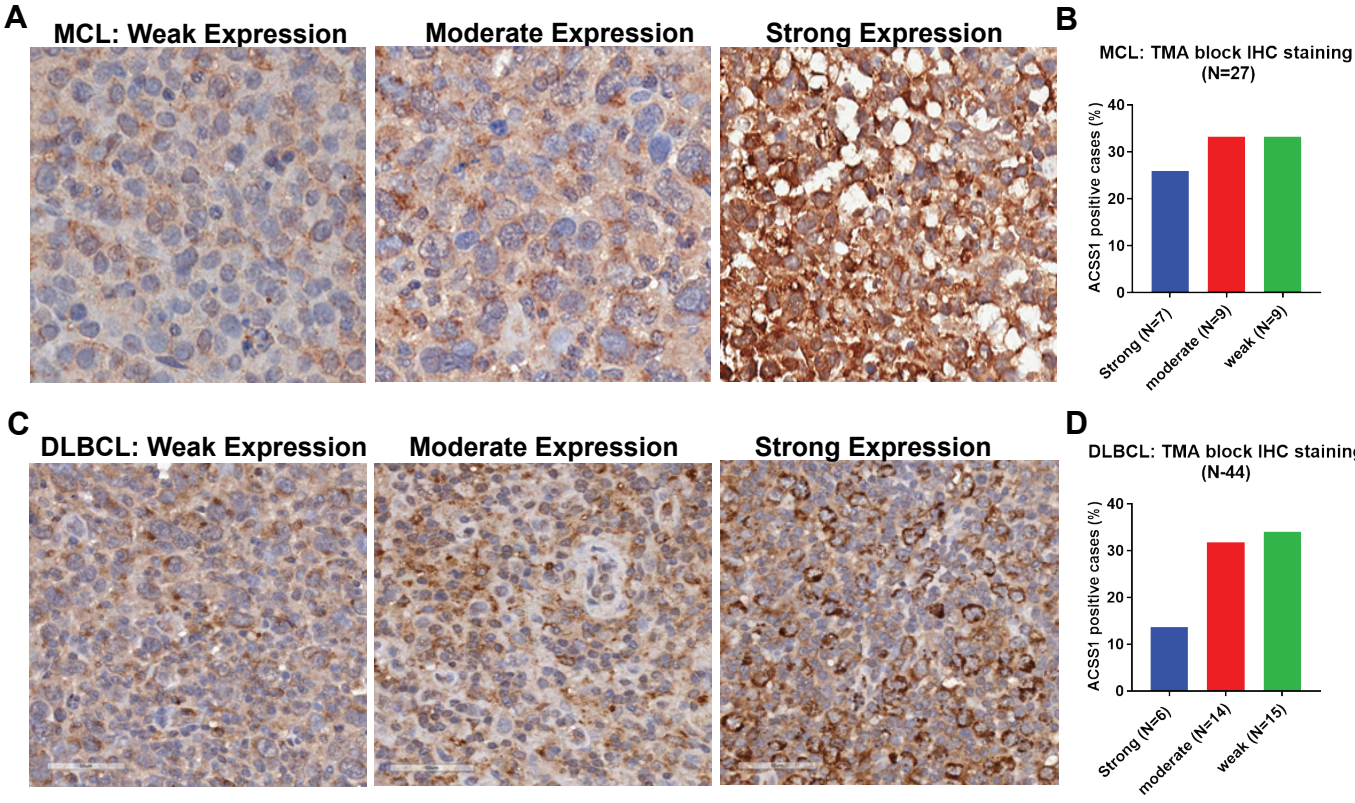
A
MCL: Weak Expression
Moderate Expression
Strong Expression
B
MCL: TMA block IHC staining
(N=27)
ACSS1 positive cases (%)
0
10
20
30
40
Strong (N=7)
moderate (N=9)
weak (N=9)
C
DLBCL: Weak Expression
Moderate Expression
Strong Expression
D
DLBCL: TMA block IHC staining
(N-44)
ACSS1 positive cases (%)
0
10
20
30
40
Strong (N=6)
moderate (N=14)
weak (N=15)

Fig.2

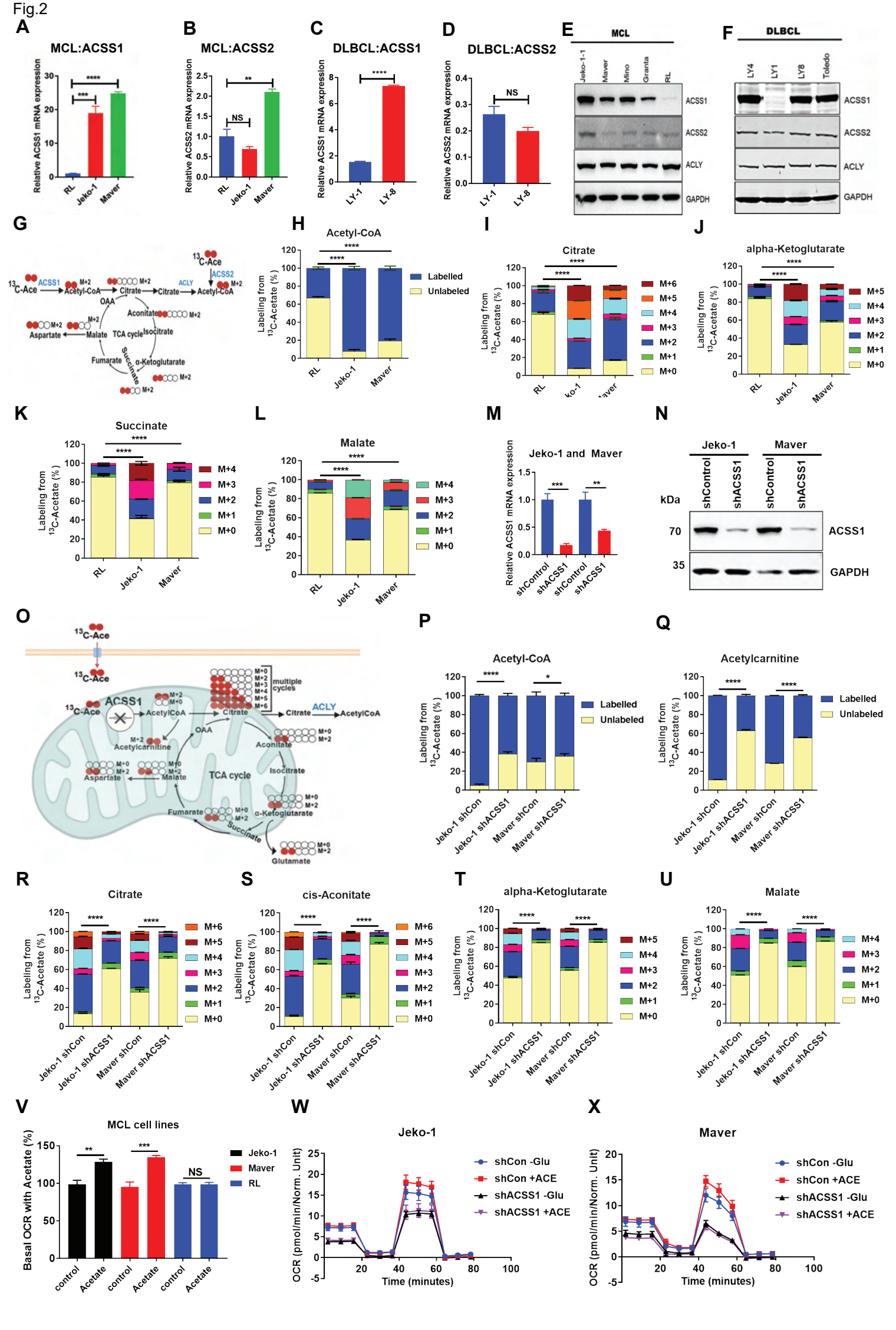
A
MCL:ACSS1
Relative ACSS1 mRNA expression
RL
Jeko-1
Maver
B
MCL:ACSS2
Relative ACSS2 mRNA expression
NS
C
DLBCL:ACSS1
Relative ACSS1 mRNA expression
LY-1
LY-8
D
DLBCL:ACSS2
Relative ACSS2 mRNA expression
E
MCL
Jeko-1
Maver
Mino
Granta
RL
ACSS1
ACSS2
ACLY
GAPDH
F
DLBCL
LY4
LY1
LY8
Toledo
G
ACSS1
ACSS2
ACLY
Acetyl-CoA
Citrate
OAA
Aconitate
Isocitrate
α-Ketoglutarate
Succinate
Fumarate
Malate
Aspartate
TCA cycle
H
Acetyl-CoA
Labelled
Unlabeled
I
Citrate
J
alpha-Ketoglutarate
K
Succinate
L
Malate
M
Jeko-1 and Maver
Relative ACSS1 mRNA expression
shControl
shACSS1
N
Jeko-1
Maver
kDa
70
35
ACSS1
GAPDH
O
multiple cycles
Acetylcarnitine
Glutamate
P
Acetyl-CoA
Jeko-1 shCon
Jeko-1 shACSS1
Maver shCon
Maver shACSS1
Q
Acetylcarnitine
R
Citrate
S
cis-Aconitate
T
alpha-Ketoglutarate
U
Malate
V
MCL cell lines
Basal OCR with Acetate (%)
control
Acetate
W
Jeko-1
OCR (pmol/min/Norm. Unit)
Time (minutes)
shCon -Glu
shCon +ACE
shACSS1 -Glu
shACSS1 +ACE
X
Maver

Fig. 3

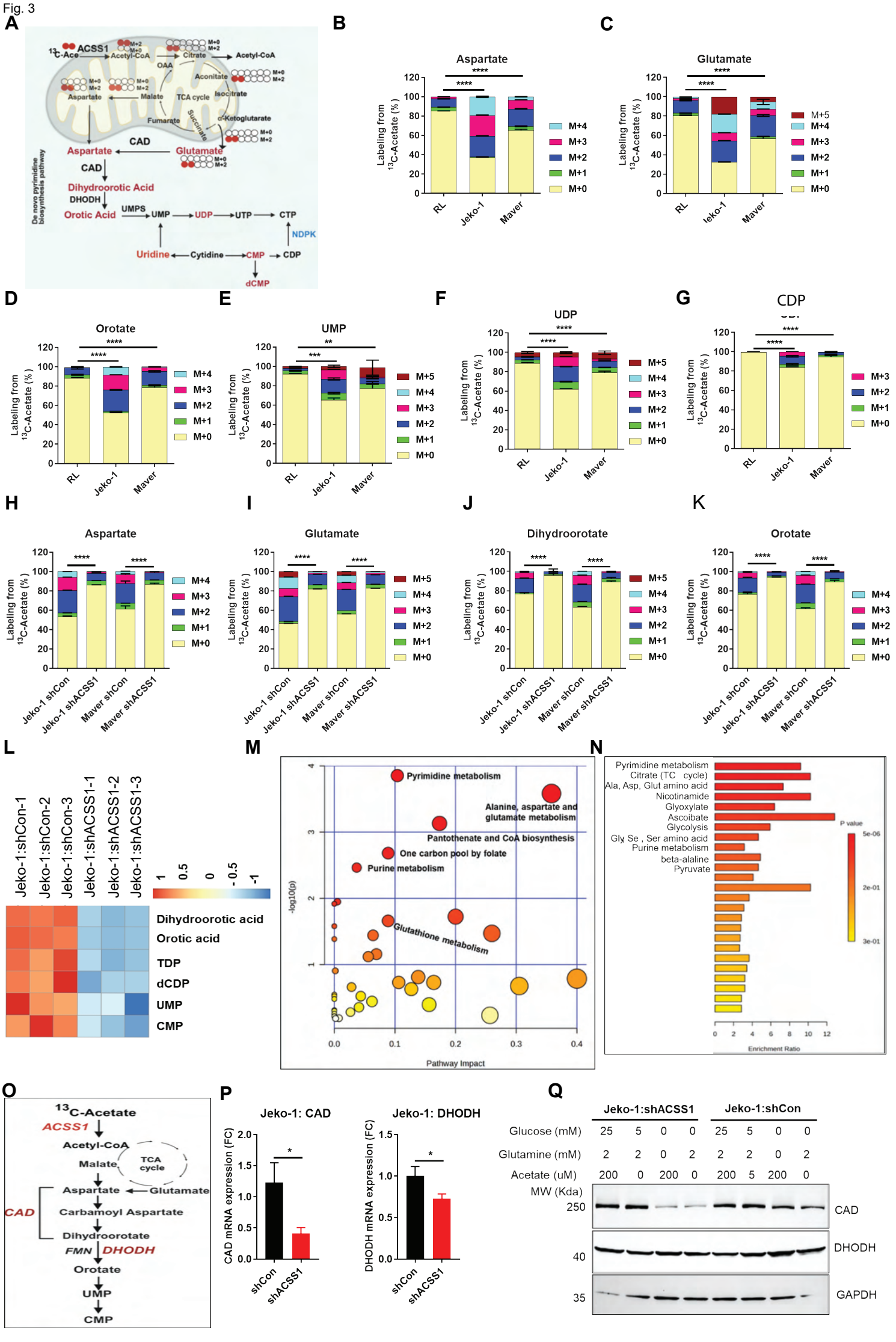
A
ACSS1
Acetyl-CoA
Citrate
Acetyl-CoA
OAA
Aconitate
Isocitrate
Aspartate
Malate
TCA cycle
Fumarate
Succinate
α-Ketoglutarate
CAD
Aspartate
Glutamate
CAD
Dihydroorotic Acid
DHODH
Orotic Acid
UMPS
UMP
UDP
UTP
CTP
NDPK
Uridine
Cytidine
CMP
CDP
dCMP
De novo pyrimidine biosynthesis pathway
B
Aspartate
C
Glutamate
Labeling from 13C-Acetate (%)
RL
Jeko-1
Maver
M+5
M+4
M+3
M+2
M+1
M+0
D
Orotate
E
UMP
F
UDP
G
CDP
H
Aspartate
I
Glutamate
J
Dihydroorotate
K
Orotate
Jeko-1 shCon
Jeko-1 shACSS1
Maver shCon
Maver shACSS1
L
Jeko-1:shCon-1
Jeko-1:shCon-2
Jeko-1:shCon-3
Jeko-1:shACSS1-1
Jeko-1:shACSS1-2
Jeko-1:shACSS1-3
Dihydroorotic acid
Orotic acid
TDP
dCDP
UMP
CMP
M
Pyrimidine metabolism
Alanine, aspartate and glutamate metabolism
Pantothenate and CoA biosynthesis
One carbon pool by folate
Purine metabolism
Glutathione metabolism
-log10(p)
Pathway Impact
N
Pyrimidine metabolism
Citrate (TC cycle)
Ala, Asp, Glut amino acid
Nicotinamide
Glyoxylate
Ascoibate
Glycolysis
Gly, Se , Ser amino acid
Purine metabolism
beta-alaline
Pyruvate
P value
Enrichment Ratio
O
13C-Acetate
ACSS1
Acetyl-CoA
Malate
TCA cycle
Aspartate
Glutamate
CAD
Carbamoyl Aspartate
Dihydroorotate
FMN
DHODH
Orotate
UMP
CMP
P
Jeko-1: CAD
Jeko-1: DHODH
CAD mRNA expression (FC)
DHODH mRNA expression (FC)
shCon
shACSS1
Q
Jeko-1:shACSS1
Jeko-1:shCon
Glucose (mM)
Glutamine (mM)
Acetate (uM)
MW (Kda)
250
40
35
CAD
DHODH
GAPDH

Fig. 4

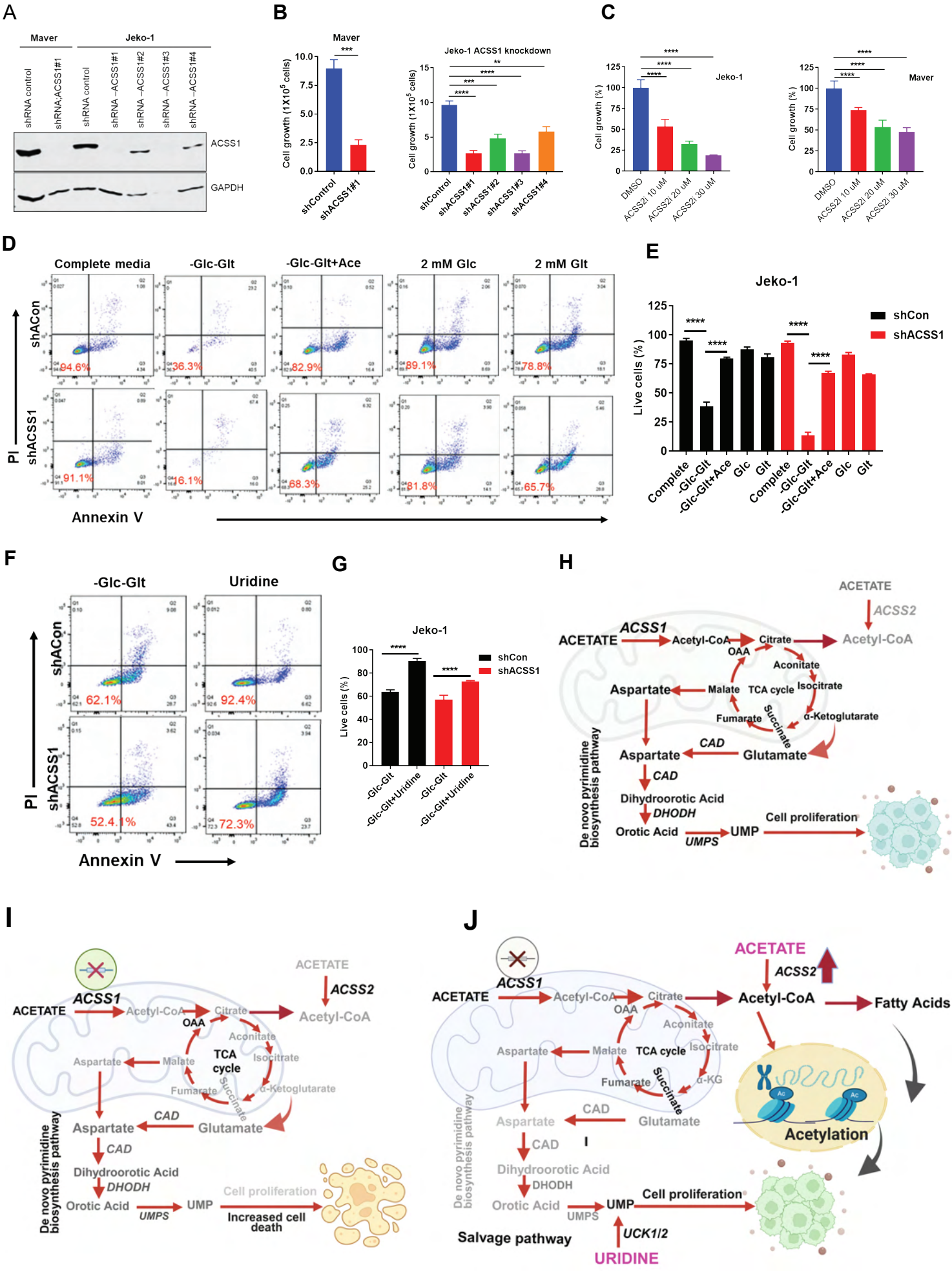
A
Maver
Jeko-1
shRNA control
shRNA:ACSS1#1
shRNA control
shRNA –ACSS1#1
shRNA –ACSS1#2
shRNA –ACSS1#3
shRNA –ACSS1#4
ACSS1
GAPDH
B
Maver
Cell growth (1X10^5 cells)
shControl
shACSS1#1
Jeko-1 ACSS1 knockdown
shACSS1#2
shACSS1#3
shACSS1#4
C
Jeko-1
Maver
Cell growth (%)
DMSO
ACSS2i 10 uM
ACSS2i 20 uM
ACSS2i 30 uM
D
Complete media
-Glc-Glt
-Glc-Glt+Ace
2 mM Glc
2 mM Glt
shACon
shACSS1
PI
Annexin V
94.6%
36.3%
82.9%
89.1%
78.8%
91.1%
16.1%
68.3%
81.8%
65.7%
E
Jeko-1
shCon
shACSS1
Live cells (%)
Complete
-Glc-Glt
-Glc-Glt+Ace
Glc
Glt
F
-Glc-Glt
Uridine
shACon
shACSS1
PI
Annexin V
62.1%
92.4%
52.4.1%
72.3%
G
Jeko-1
shCon
shACSS1
Live cells (%)
-Glc-Glt
-Glc-Glt+Uridine
H
ACETATE
ACSS1
ACSS2
Acetyl-CoA
Citrate
OAA
Aconitate
Isocitrate
α-Ketoglutarate
Succinate
Fumarate
Malate
TCA cycle
Aspartate
Glutamate
CAD
Dihydroorotic Acid
DHODH
Orotic Acid
UMPS
UMP
Cell proliferation
De novo pyrimidine biosynthesis pathway
I
ACETATE
ACSS1
ACSS2
Acetyl-CoA
Citrate
OAA
Aconitate
Isocitrate
α-Ketoglutarate
Succinate
Fumarate
Malate
TCA cycle
Aspartate
Glutamate
CAD
Dihydroorotic Acid
DHODH
Orotic Acid
UMPS
UMP
Cell proliferation
Increased cell death
De novo pyrimidine biosynthesis pathway
J
ACETATE
ACSS1
ACSS2
Acetyl-CoA
Fatty Acids
Citrate
OAA
Aconitate
Isocitrate
α-KG
Succinate
Fumarate
Malate
TCA cycle
Aspartate
Glutamate
CAD
Dihydroorotic Acid
DHODH
Orotic Acid
UMPS
UMP
Cell proliferation
Acetylation
Salvage pathway
UCK1/2
URIDINE
De novo pyrimidine biosynthesis pathway

Fig. 5

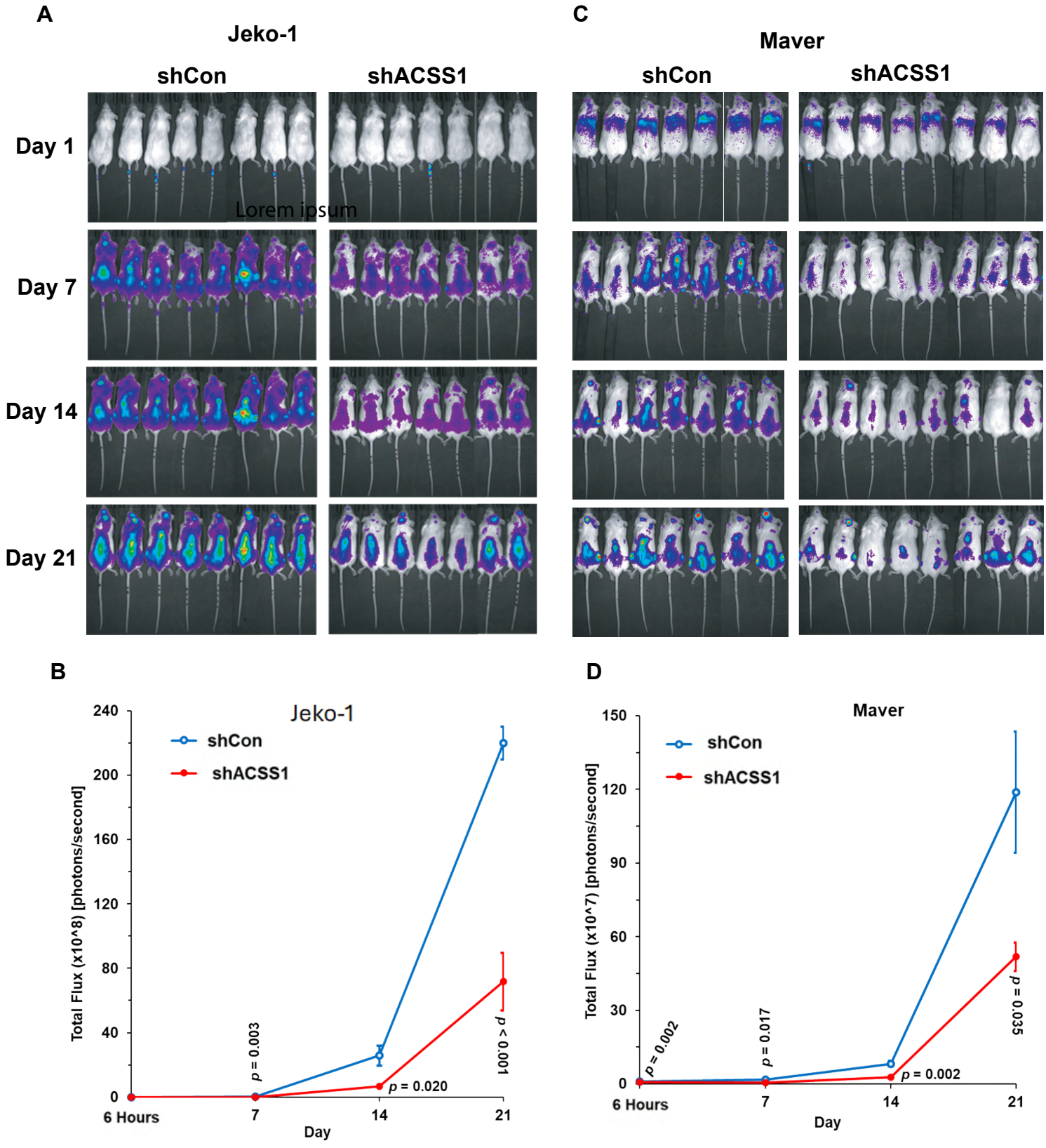
A
Jeko-1
shCon
shACSS1
Day 1
Day 7
Day 14
Day 21
Lorem ipsum
C
Maver
shCon
shACSS1
B
Jeko-1
shCon
shACSS1
Total Flux (x10^8) [photons/second]
240
200
160
120
80
40
0
6 Hours
7
14
21
Day
p = 0.003
p = 0.020
p < 0.001
D
Maver
shCon
shACSS1
Total Flux (x10^7) [photons/second]
150
120
90
60
30
0
6 Hours
7
14
21
Day
p = 0.002
p = 0.017
p = 0.002
p = 0.035

Supplementary Fig. 1

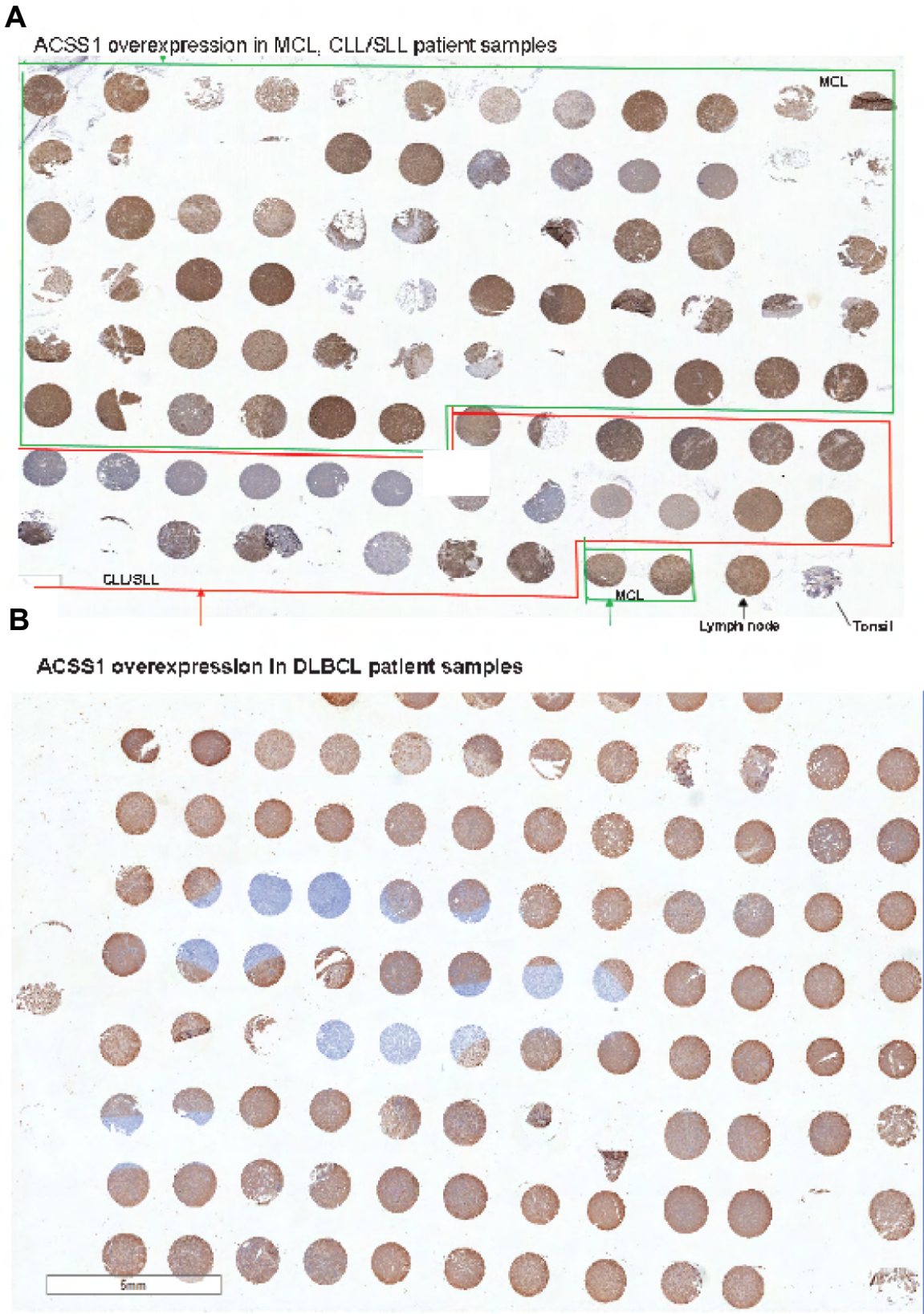

Immunohistochemistry (IHC) staining of ACSS1 in patients with MCL, DLBCL, and CLL biopsies.

A ACSS1 overexpression in MCL, CLL/SLL patient samples; **B** ACSS1 overexpression in DLBCL patient samples.

Supplementary Fig. 2

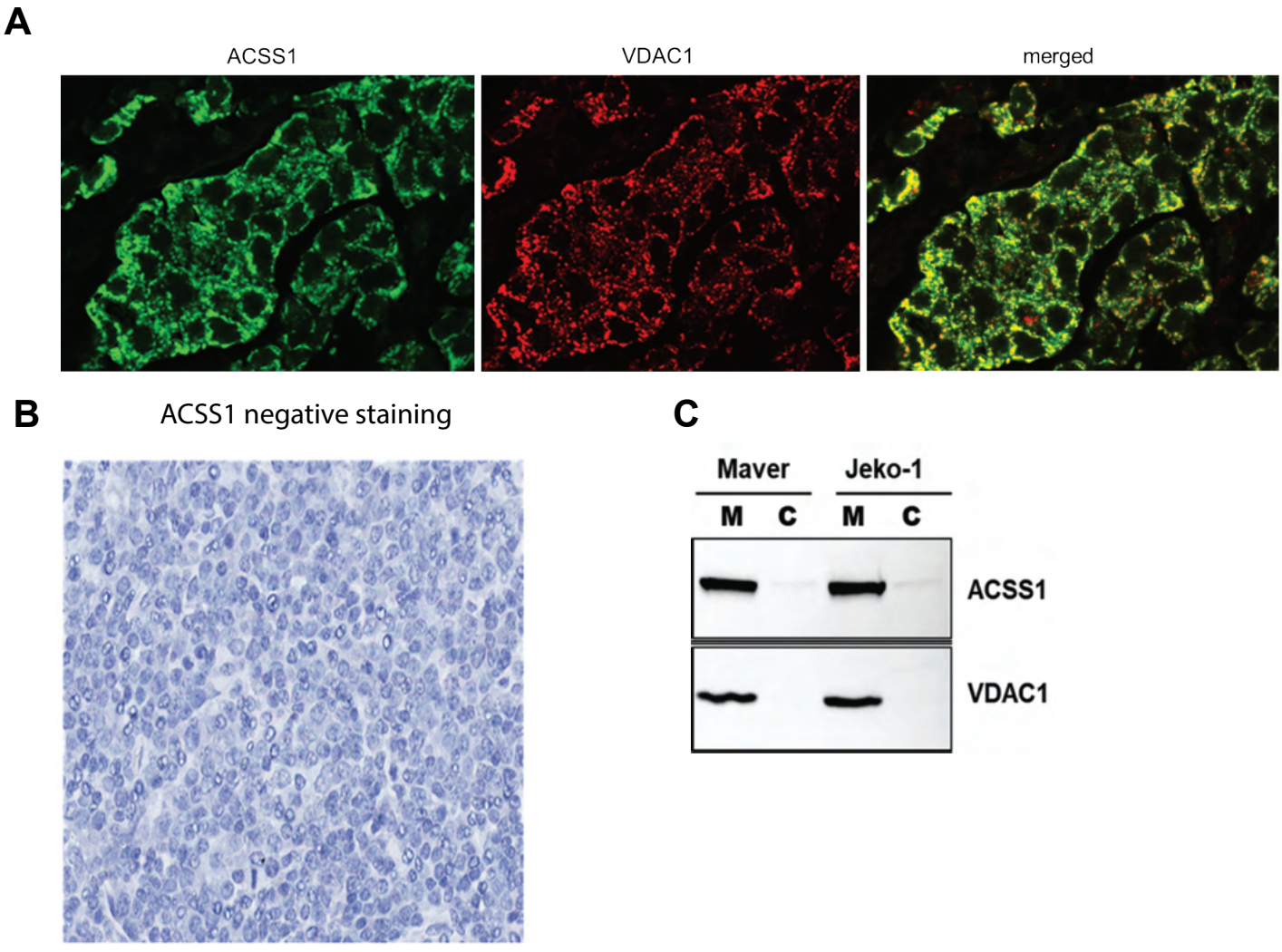

ACSS1 and VDAC1 co-localization in mitochondria.

A, Immunofluorescence (IF) on a human breast cancer patient sample with ACSS1 and VDAC1 staining, followed by confocal microscopy. **B**,Immunohistochemistry (IHC) negative staining of ACSS1 in MCL, DLBCL, and ALCL patient-derived TMA blocks. **C**, Mitochondrial fractionation of Jeko-1 and Maver cells.

Supplementary Fig. 3

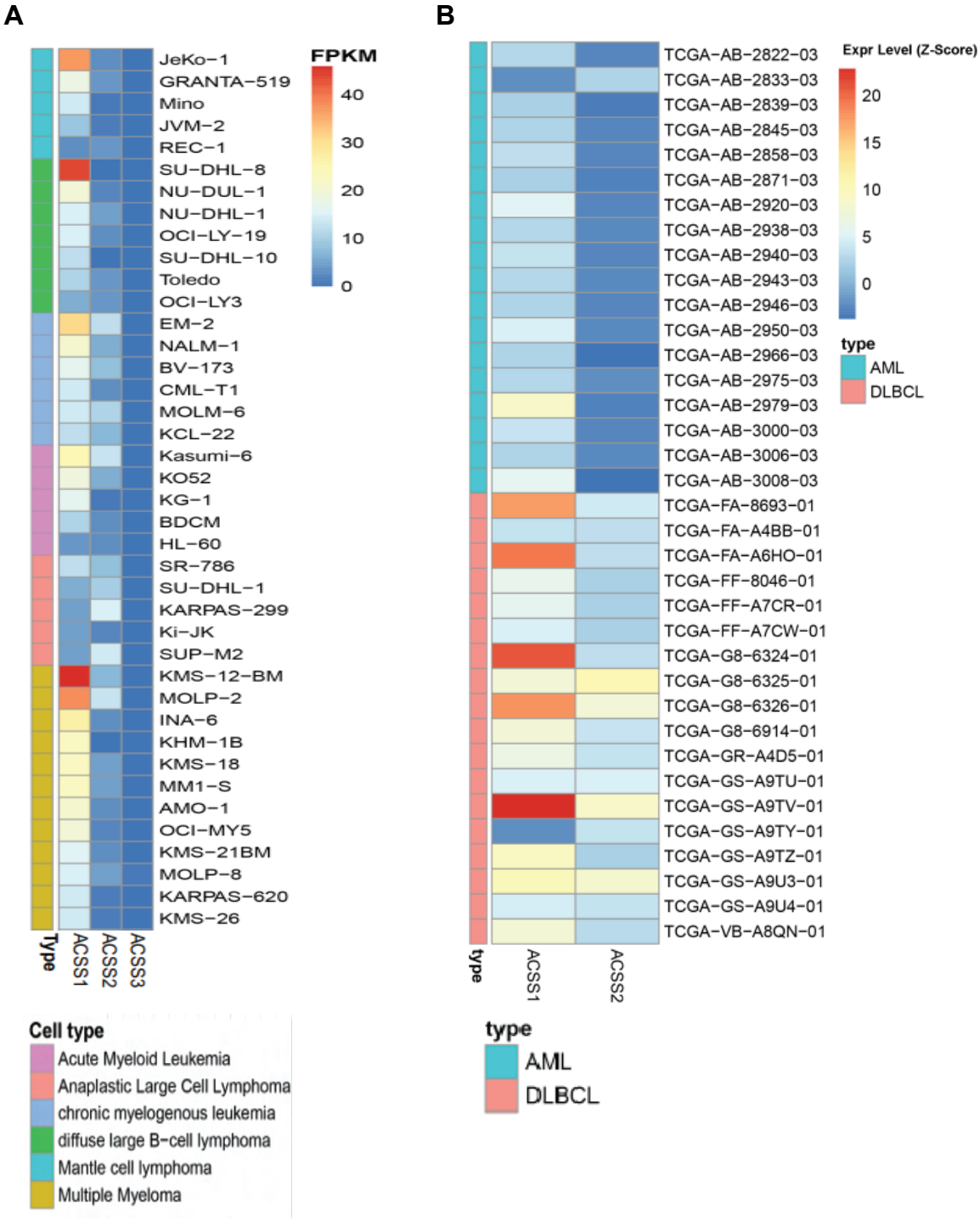

ACSS1 is overexpressed in cell lines and primary tissues derived from hematological malignancies.

A Targeted bioinformatics analysis of ACSS1, ACSS2, and ACSS3 gene expression deposited in the Expression Atlas database (https://www.ebi.ac.uk/gxa/home) revealed overexpression of ACSS1 in cell lines derived from human hematological malignancies (heat map); **B** The Cancer Genome Atlas (TCGA) database revealed ACSS1 overexpression in primary AML and DLBCL tissues.

Supplementary Fig. 4

A

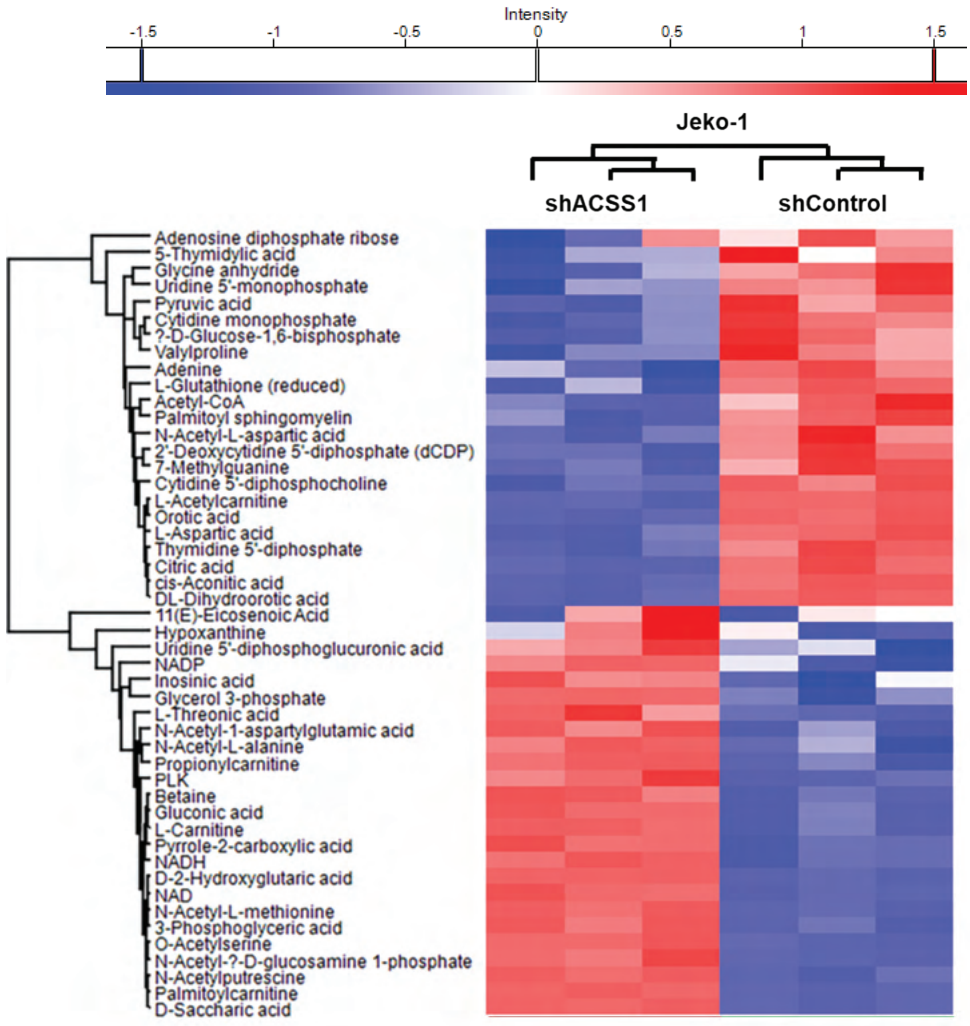

B

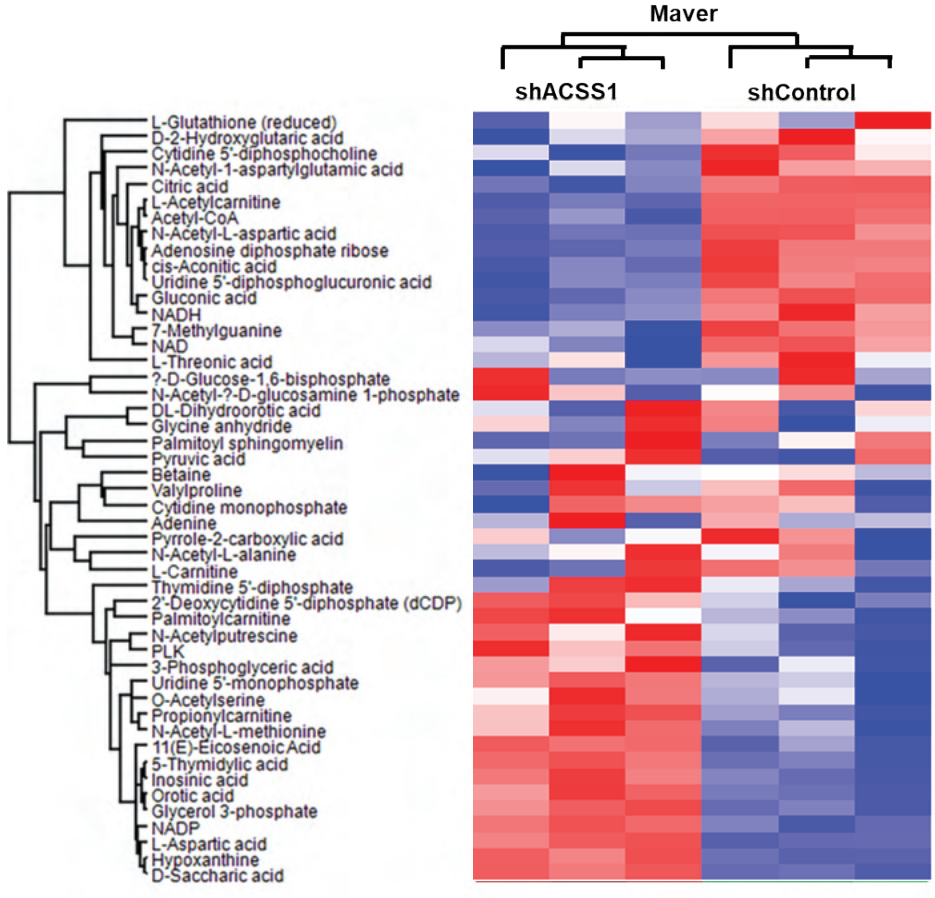

The steady-state metabolites significantly differed in Jeko-1 control compared to ACSS1 KD cell lines during nutrient deprivation.

a, b The heat map shows a statistically significant metabolite in shCon vs. shACSS1 in Jeko-1 and Maver cell lines.